NASA/TM—2020-220467

LCF Life of NiCr-Y Coated Disk Alloys After Shot Peening, Oxidation and Hot Corrosion

James A. Nesbitt, Robert A. Miller, Timothy P. Gabb, and Susan L. Draper
Glenn Research Center, Cleveland, Ohio

Ivan E. Locci
University of Toledo, Toledo, Ohio

Chantal K. Sudbrack
Glenn Research Center, Cleveland, Ohio

March 2020

NASA STI Program . . . in Profile

Since its founding, NASA has been dedicated to the advancement of aeronautics and space science. The NASA Scientific and Technical Information (STI) Program plays a key part in helping NASA maintain this important role.

The NASA STI Program operates under the auspices of the Agency Chief Information Officer. It collects, organizes, provides for archiving, and disseminates NASA's STI. The NASA STI Program provides access to the NASA Technical Report Server—Registered (NTRS Reg) and NASA Technical Report Server—Public (NTRS) thus providing one of the largest collections of aeronautical and space science STI in the world. Results are published in both non-NASA channels and by NASA in the NASA STI Report Series, which includes the following report types:

- TECHNICAL PUBLICATION. Reports of completed research or a major significant phase of research that present the results of NASA programs and include extensive data or theoretical analysis. Includes compilations of significant scientific and technical data and information deemed to be of continuing reference value. NASA counter-part of peer-reviewed formal professional papers, but has less stringent limitations on manuscript length and extent of graphic presentations.

- TECHNICAL MEMORANDUM. Scientific and technical findings that are preliminary or of specialized interest, e.g., "quick-release" reports, working papers, and bibliographies that contain minimal annotation. Does not contain extensive analysis.

- CONTRACTOR REPORT. Scientific and technical findings by NASA-sponsored contractors and grantees.

- CONFERENCE PUBLICATION. Collected papers from scientific and technical conferences, symposia, seminars, or other meetings sponsored or co-sponsored by NASA.

- SPECIAL PUBLICATION. Scientific, technical, or historical information from NASA programs, projects, and missions, often concerned with subjects having substantial public interest.

- TECHNICAL TRANSLATION. English-language translations of foreign scientific and technical material pertinent to NASA's mission.

For more information about the NASA STI program, see the following:

- Access the NASA STI program home page at http://www.sti.nasa.gov

- E-mail your question to help@sti.nasa.gov

- Fax your question to the NASA STI Information Desk at 757-864-6500

- Telephone the NASA STI Information Desk at 757-864-9658

- Write to:
  NASA STI Program
  Mail Stop 148
  NASA Langley Research Center
  Hampton, VA 23681-2199

NASA/TM—2020-220467

LCF Life of NiCr-Y Coated Disk Alloys After Shot Peening, Oxidation and Hot Corrosion

James A. Nesbitt, Robert A. Miller, Timothy P. Gabb, and Susan L. Draper
Glenn Research Center, Cleveland, Ohio

Ivan E. Locci
University of Toledo, Toledo, Ohio

Chantal K. Sudbrack
Glenn Research Center, Cleveland, Ohio

National Aeronautics and
Space Administration

Glenn Research Center
Cleveland, Ohio 44135

March 2020

This work was sponsored by the Advanced Air Vehicle Program
at the NASA Glenn Research Center

Level of Review: This material has been technically reviewed by technical management.

Available from

NASA STI Program
Mail Stop 148
NASA Langley Research Center
Hampton, VA 23681-2199

National Technical Information Service
5285 Port Royal Road
Springfield, VA 22161
703-605-6000

This report is available in electronic form at http://www.sti.nasa.gov/ and http://ntrs.nasa.gov/

LCF Life of NiCr-Y Coated Disk Alloys After Shot Peening, Oxidation and Hot Corrosion

James A. Nesbitt*, Robert A. Miller*, Timothy P. Gabb, and Susan L. Draper*
National Aeronautics and Space Administration
Glenn Research Center
Cleveland, Ohio 44135

Ivan E. Locci
University of Toledo
Toledo, Ohio 43606

Chantal K. Sudbrack†
National Aeronautics and Space Administration
Glenn Research Center
Cleveland, Ohio 44135

Abstract

In a prior companion study (Ref. 1), three different Ni-Cr coating compositions (29, 35.5, 45 wt% Cr) were applied at two thicknesses by Plasma Enhanced Magnetron Sputtering (PEMS) to two similar Ni-based disk alloys. One coating also received a thin ZrO_2 overcoat. The low cycle fatigue (LCF) life of each coating was determined at 760 °C and was less than that of the uncoated specimens. In this follow-on effort, shot peening was examined as a means to improve the as-deposited coating morphology as well as impart a residual compressive stress in the near-surface region. After evaluating the effect of the shot peening on the LCF life, the effectiveness of the shot-peened coating in protecting the disk alloy from oxidation and hot corrosion attack was evaluated. This evaluation was accomplished by exposing coated and shot-peened specimens to 500 h of oxidation followed by 50 h of hot corrosion, both at 760 °C in air. These exposed specimens were then tested in fatigue and compared to similarly treated and exposed uncoated specimens. For all cases, shot peening improved the LCF life of the coated specimens. More specifically, the highest Cr coating showed the best LCF life of the coated specimens after shot peening, as well as after the environmental exposures. Characterization of the coatings after shot peening, oxidation, hot corrosion and LCF testing is presented and discussed.

Introduction

In a prior study (Ref. 1), the low cycle fatigue (LCF) lives of three different Ni-Cr-Y coating compositions were measured at 760 °C. The coatings were applied by Plasma Enhanced Magnetron Sputtering (PEMS) to two similar Ni-based disk alloys. Two of the coating compositions were applied at two thicknesses. One coating also received a thin ZrO_2 overcoat. The coated specimens were given a short diffusion annealing heat treatment in a low PO_2 environment to improve the bond between the coating and substrate as well as to encourage Cr_2O_3 formation prior to LCF testing. In Reference 1, it was found that the presence of the coating reduced the LCF life of the disk alloys such that the LCF lives of

*Retired
†Formerly with NASA Glenn Research Center

all coated specimens were lower than those of uncoated specimens. Comparing among the coated specimens only, the LCF life increased with increasing Cr content of the coating. As observed in other studies, there was significantly more secondary cracking in the coating than in the uncoated substrate, and this cracking increased with Cr content of the coating. Although there was significantly more secondary cracking in the coatings, most of the cracks were arrested at the substrate.

It is well known that defects such as casting porosity or nonmetallic inclusions often initiate the primary failure crack during LCF testing, especially when those defects are at the surface (Refs. 2 to 5). In Reference 1, two types of surface defects in the coatings significantly impacted the fatigue life by creating crack initiation sites at the surface. The most damaging defects were "spits" which deposit on the surface via the ejection of molten droplets (Ref. 6) and were weakly bonded to the coating. Some of the spits were lost from the coating creating large "pinhole" defects (Ref. 6). These spits and holes, commonly associated with PVD coatings, were prime sites for crack initiation and were often observed on the fracture surface at the initiation site for the primary crack. The second coating defect, aligned along the LCF load axis, resulted from the growth of the coating reflecting longitudinal polishing marks on the surface of the LCF specimens. These defects, termed "linear gaps" to distinguish them from fatigue cracks, had the appearance of a crack, and although aligned with the specimen load axis, appeared to initiate some primary fatigue cracks.

Hence, in this current study, shot peening the surface of the coated specimens was performed to plastically deform the coating surface in an attempt to close the linear gaps, and secondly, to attempt to bond the spits to the coating. In addition, it is well known that shot peening imparts a near-surface compressive stress in a component which is beneficial in reducing surface cracking due to surface defects (e.g., exposed inclusions) during LCF testing (Refs. 4, 5, 7, and 8). Therefore, the peening was expected to also have an additional beneficial effect due to this residual compressive stress. However, the benefit of the compressive stress can be reduced by thermal exposures prior to, or during LCF testing (Refs. 9 to 12). Recent work with the same high-Cr coating as in the present study showed that both the coating and adjacent substrate were compressively loaded after shot peening with residual stresses similar to those of an uncoated specimen. However, after a short diffusion anneal, all of the compressive residual stress in the coating was relieved and the coating showed a slight tensile residual stress at room temperature, probably due to the CTE mismatch between the coating and substrate (Ref. 13). Fortunately, some of the compressive residual stress remained in the substrate. Therefore, there was uncertainty about the residual stress benefit from shot peening.

The overall purpose of this study was to determine the ability of NiCr-Y coatings to protect disk alloys from oxidation and hot corrosion attack without degrading the LCF life. Reference 1 examined the effect of the presence of the coating (including a short diffusion anneal) on the LCF life. The purpose of the present study was to determine the effect shot peening, as well as the effect of oxidation and hot corrosion on the LCF life of the coatings. This study was divided into two steps. Firstly, the effect of shot peening followed by a short diffusion anneal on the LCF life was determined. This first step of the study involved determining both the effectiveness of shot peening in mitigating the detrimental effects of the surface defects associated with the coating deposition (i.e., the linear gaps and spits observed in Reference 1), as well as any beneficial effect of the near-surface compressive residual stress imparted by the shot peening. The second step was to determine the effect of oxidation and hot corrosion attack on the LCF life of the peened coatings. In order to determine the overall benefit of the coatings in protecting the disk alloy from oxidation and hot corrosion attack, uncoated specimens were also shot peened, oxidized, hot corroded and tested alongside the coated specimens.

Experimental Procedures

Details regarding the substrate composition, fabrication, and LCF specimen geometry were given in Reference 1. Although two similar disk alloys were used in the initial studies presented in Reference 1, only the ME3 alloy was used in the present study. The three coating compositions, thicknesses and details of the deposition process, were also given in Reference 1 as well as the justification behind the choice of NiCr-Y coatings. For convenience, the coating designations, thicknesses and deposited coating compositions from Reference 1 are reproduced below in Table 1. In addition to the LCF specimens, 1-2 characterization pins of the ME3 alloy had also been coated with each set of LCF specimens and were utilized in the present study. Polished cross-sections of the coating microstructure and images of the surface morphology after coating deposition and again after LCF testing, were shown in Reference 1.

Shot Peening

Shot peening of the coated, and the uncoated specimens and pins was performed at Metal Improvement Co. of Blue Ash, Ohio using conditioned cut stainless steel wire (CCW14) with a roughly spherical mean diameter of 360 μm (0.014 in.). Shot peening intensity was 16N with a coverage of 200 percent. The 200 percent coverage is defined as twice the shot peening time needed to indent all of the exposed area once.

Low PO_2 Diffusion Anneal

Following shot peening, the LCF specimens and pins, coated and uncoated, were given a short thermal anneal at 760 °C for 8 h in an environment with a low partial pressure of oxygen. The purpose for this anneal was two-fold, firstly, to allow some interdiffusion and bonding between the coating and substrate prior to further processing, and secondly, to promote the formation of a Cr_2O_3 scale on the coating surface. The partial pressure of oxygen during this anneal was approximately 1.4×10^{-15} atm at which only the Cr and Y would oxidize on the surface of the coating. After the shot peening and anneal, the specimen or pin surfaces were examined using a scanning electron microscope (SEM) using either secondary electron (SE) or backscattered electron (BSE) imaging. Further details of this low PO_2 anneal are given in Reference 1.

TABLE 1.—RUN DESIGNATION, TARGETS, COATING THICKNESS AND DEPOSITED COATING CR CONTENT IN WEIGHT PERCENT (wt%)

Coating designation	Target 1, wt%	Target 2, wt%	Coating thickness,[a] μm	Deposited coating Cr content,[b] wt%	Coating Run ID
Low Cr*, *Thin	Ni-27.3Cr-0.12Y[c]	----------	20.4±0.6	29.1	NM1
Med Cr*, *Thin	Ni-27.3Cr-0.12Y	100% Cr	21.5±0.9	37.0	NM2
High Cr*, *Thin	Ni-27.3Cr-0.12Y	100% Cr	19.8±1.9	44.4	NM4
Low Cr*, *Thick	Ni-27.3Cr-0.12Y	----------	37.6±4.2	28.9	NM3
Med Cr*, *Thick	Ni-27.3Cr-0.12Y	100% Cr	41.0±0.8	35.2	NM6
Med Cr+ZrO_2*, *Thin	Ni-35Cr-0.15Y[d]	100% Zr[e]	19.3±1.0	34.8	NM7

[a]Thickness measured on pins after 16N-200 percent shot peen and 8 h low PO_2 diffusion anneal
[b]Composition measured by EDS
[c]Analyzed composition, nominal given as Ni-28Cr-0.15Y
[d]Nominal composition
[e]Oxygen was introduced into the chamber to reactively sputter a thin ZrO_2 layer

Oxidation and Hot Corrosion Testing

Specimens, coated and uncoated, and coated characterization pins underwent oxidation exposure for 500 h at 760 °C in static lab air. Although there were pins coated with the ***Low Cr***, ***Thin*** coating available for oxidation and characterization, no coated LCF specimens of this composition were available for the oxidation or following hot corrosion testing. After oxidation, the surfaces of the characterization pins were examined in the SEM, then sectioned perpendicular to the pin axis, mounted, polished and examined optically or by SEM. Following the oxidation exposure, the LCF specimens were hot corrosion tested by applying a corrosive salt to the specimen surface and exposing the salt-coated specimen at 760 °C for 50 h in static lab air. The salt composition was 72% Na_2SO_4-28% $MgSO_4$ (wt%). This binary Na_2SO_4-$MgSO_4$ salt was selected based on corrosion pit formation in earlier hot corrosion studies of an uncoated disk alloy (Ref. 14). In addition, earlier testing at 700 and 760 °C in air showed that this salt composition produced a desirable discrete pit morphology in uncoated disk materials (Ref. 15). The point of first liquid formation for this salt is approximately 730 °C (Ref. 16).

The salt was prepared into a paste and applied to a 1 cm length around the test section of the LCF specimen. Salt loading, after the burn off of the liquid paste binder at 400 °C for 1 h, was intended to be 2 mg/cm^2. Because of the difficulty in applying the salt paste, the salt loading varied from 1.9 to 5.2 mg/cm^2. Two LCF specimens with the dried salt were placed horizontally in an alumina boat. An uncoated witness coupon of the LSHR alloy was also prepared in an identical manner and also tested horizontally in the alumina boat with each set of LCF specimens. This witness coupon confirmed the presence of hot corrosion conditions by showing the presence of corrosion pits on the uncoated specimen surface.

The furnace used for the hot corrosion testing was a horizontal tube furnace operated in static lab air. While the furnace was held at 740 °C, the alumina boat and specimens were quickly slid into the hot section of the furnace. The furnace controller was slowly increased over a period of approximately 15 min to bring the furnace to the test temperature of 760 °C without any significant temperature overshoot. The test time was initiated when the furnace reached the test temperature and was continued at that temperature for 50 h. After 50 h, the alumina boat and specimens were quickly removed from the furnace and allowed to air cool. After cooling, the specimens were weighed and the surfaces of selected specimens were examined in the SEM. After this examination, the corroded specimens were sonically cleaned in water and Alconox cleaner for approximately 8 h, which typically removed all soluble salt and loose corrosion products from the surface. After drying and re-weighing, the surfaces of selected specimens were again examined in the SEM. Following this examination, the coated and uncoated specimens were fatigue tested to failure.

LCF Testing

Fatigue cycling was conducted at 760 °C in air on all test specimens using a servo-hydraulic test machine with a resistance heated furnace integrated to enclose the specimen and specimen grips. Stress was consistently cycled between maximum and minimum stress values of 841 and –427 MPa in each cycle using a saw-tooth waveform at a frequency of 0.33 Hz. Replicates of each specimen were tested. Previous testing of uncoated ME3 at this strain range at 760 °C resulted primarily in surface initiated cracks leading to failure (Ref. 17). After testing, fracture surfaces and sides of all specimens were examined in the SEM to identify the primary crack initiation site (surface or internal). The fractured specimen was then rotated in the SEM and the side surface of the LCF specimen was examined in the same area as the primary crack initiation point. After the SEM examination, portions of the tested specimens were sectioned perpendicular and parallel to the load axis, mounted, polished and examined as in Reference 1. The perpendicular mounts show the coating microstructure and thickness while the parallel mounts allow examination of the fatigue cracks, as depicted in Reference 1. Further details of the LCF testing are given in Reference 1.

Results

The surface morphologies of the three different coating compositions were notably different after shot peening. The coating surfaces, after shot peening and low PO_2 diffusion anneal, are shown in Figure 1. More deformation was evident in the ***Low Cr*** coating than in the ***Med Cr*** or ***High Cr*** coatings (Figure 1(a) to (c)). The ***High Cr***, ***Thin*** coating appeared relatively smooth with curious oval pores on the surface (Figure 1(c)). The longitudinal polishing marks could still be distinguished on the ***Med Cr+ZrO₂ Thin*** coating (Figure 1(f)). The deformation of the ***Low Cr*** coating can be seen more clearly in the higher magnification image in Figure 1(d). Some plastic deformation is apparent on the ***Med Cr*** coating including a large dimple on the surface shown in Figure 1(e). The oval pores in the ***High Cr*** coating (Figure 1(c)) are shown at a higher magnification in Figure 2(a) and (b). A "dimple" was clearly observed around each of the pores. The large dimple shown in the ***Med Cr***, ***Thick*** coating (Figure 1(e)) is shown at a higher magnification in Figure 2(c) and (d). At the bottom of the dimple is a small hole, similar to that for the ***High Cr***, ***Thin*** coatings shown in Figure 2(a) and (b). It is likely that the shot peening knocked out some of the spits on the surface creating holes. Holes in the coating had also been observed prior to peening. The shot peening is thought to have plastically deformed and possibly filled in some of the holes. In other holes, deformation of the outer surface of the coating could have closed up some of the holes, leaving a cavity, or partial cavity behind with the small hole marking a cavity below. The surface above the cavity would offer less resistance to the shot peening and would be more easily "dented" by the impact of a shot leaving the dimple on the surface. As expected, EDS analysis on the surface of most of the specimens after shot peening and low PO_2 anneal showed high enrichment of Cr likely due to the

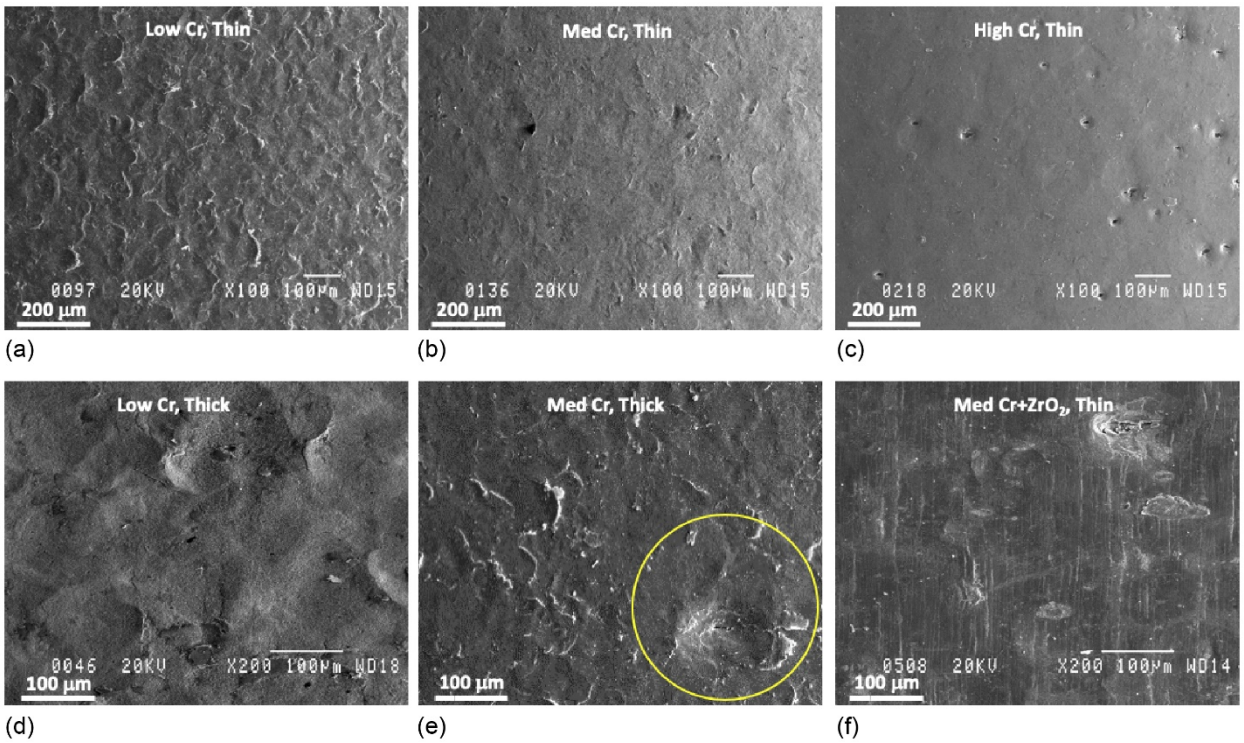

Figure 1.—SE images of the surface of the 6 coatings after shot peening and low PO_2 anneal (a-f). Significant plastic deformation is evident in the ***Low Cr*** coatings (a,d) and a very smooth surface is evident in the ***High Cr*** coating (c). A large dimple from the shot peen media is highlighted in yellow in (e). Longitudinal polishing marks are evident in the ***Med Cr+ZrO₂***, Thin coating (f). Note the difference in magnification between (a-c) and (d-f). The specimen loading axis is vertical in each of these images.

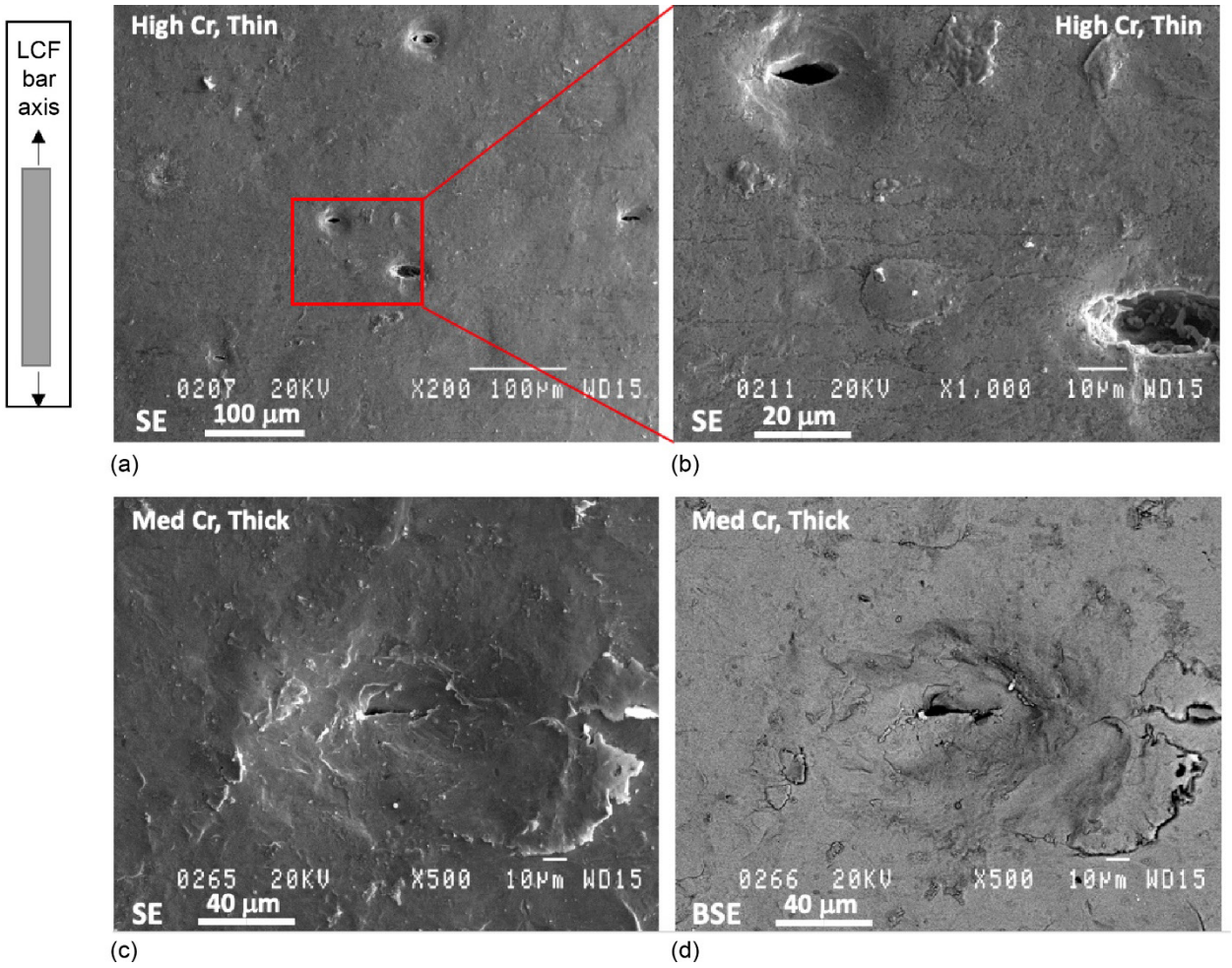

Figure 2.—(a,b) SE images of the surface of the ***High Cr, Thin*** coating after shot peening and low PO_2 anneal showing dimples over "pores" (c,d). Magnified SE and BSE images of the dimple in the ***Med Cr*** coating shown in Figure 1(e). Note the small hole or pore at the bottom of the dimple.

formation of a thin Cr_2O_3 layer on the surface. The exception was the coating with the thin ZrO_2 layer (***Med Cr+ZrO₂***) which showed a high peak for Zr as well as for Cr. At times, small peaks for Fe would be present, representing some Fe contamination on the surface from the shot peening media.

Additional views of the ***High Cr***, ***Thin*** coating are shown in Figure 3. The red circled feature on the surface is believed to be a spit flattened by the shot peening. Although hardly visible in the SE image (Figure 3(a)), small, oval-flattened spits are indicated by the yellow markers in Figure 3(b). The mottled surface of the ***Med Cr+ZrO₂*** coated specimen is shown in Figure 4(a) and (b). EDS of the surface indicated that much of the ZrO_2 layer was still intact (light regions in Figure 4(b) and (c), EDS spectra in (d)). The high Cr and Ni peaks in these Zr-rich regions are likely due to the electron beam passing through the thin ZrO_2 layer. EDS of the dark regions in Figure 4(b) and (c) indicated areas enriched in Cr, likely Cr_2O_3 (Figure 4(e)). Higher magnification views of these dark regions appeared similar to oxidized regions of the Ni-Cr coating on other specimens.

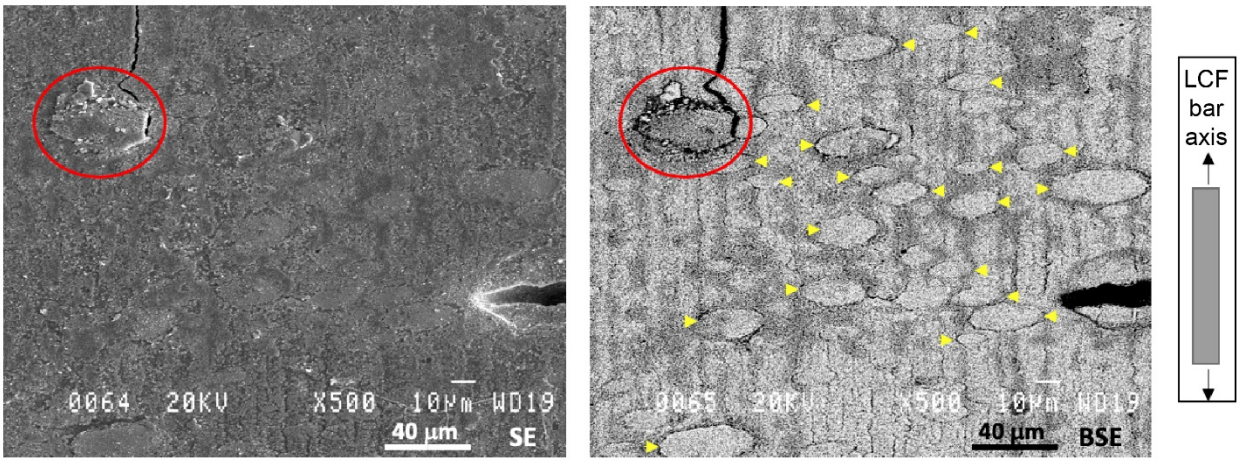

(a) (b)

Figure 3.—(a) SE and (b) BSE images of the surface of the ***High Cr, Thin*** coating after shot peening and low PO_2 anneal showing a flattened spit (red circle) and numerous, flattened smaller spits (yellow arrowheads).

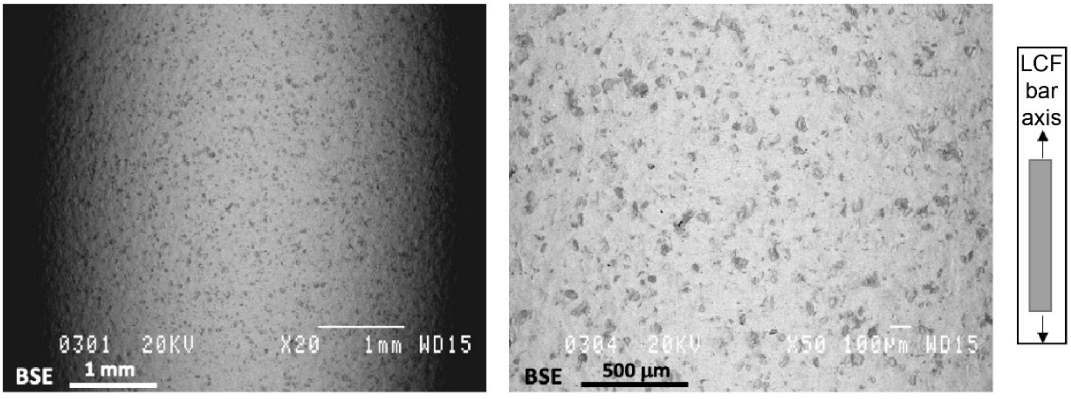

(a) (b)

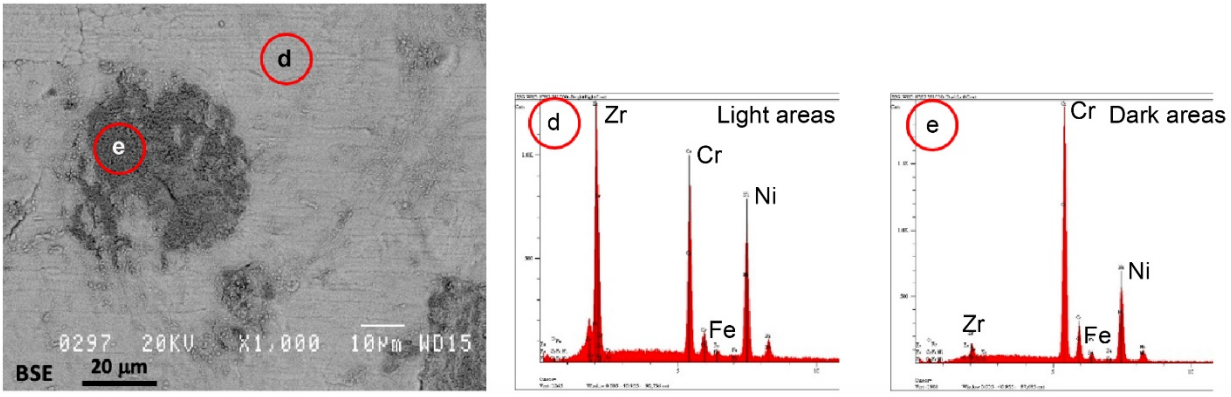

(c) (d) (e)

Figure 4.—(a,b) BSE images of the ***Med Cr+ZrO_2, Thin*** coating after shot peening and low PO_2 anneal showing a mottled surface. (c) Magnified BSE image of one of the dark regions, EDS spectra of the (d) light and (e) dark areas.

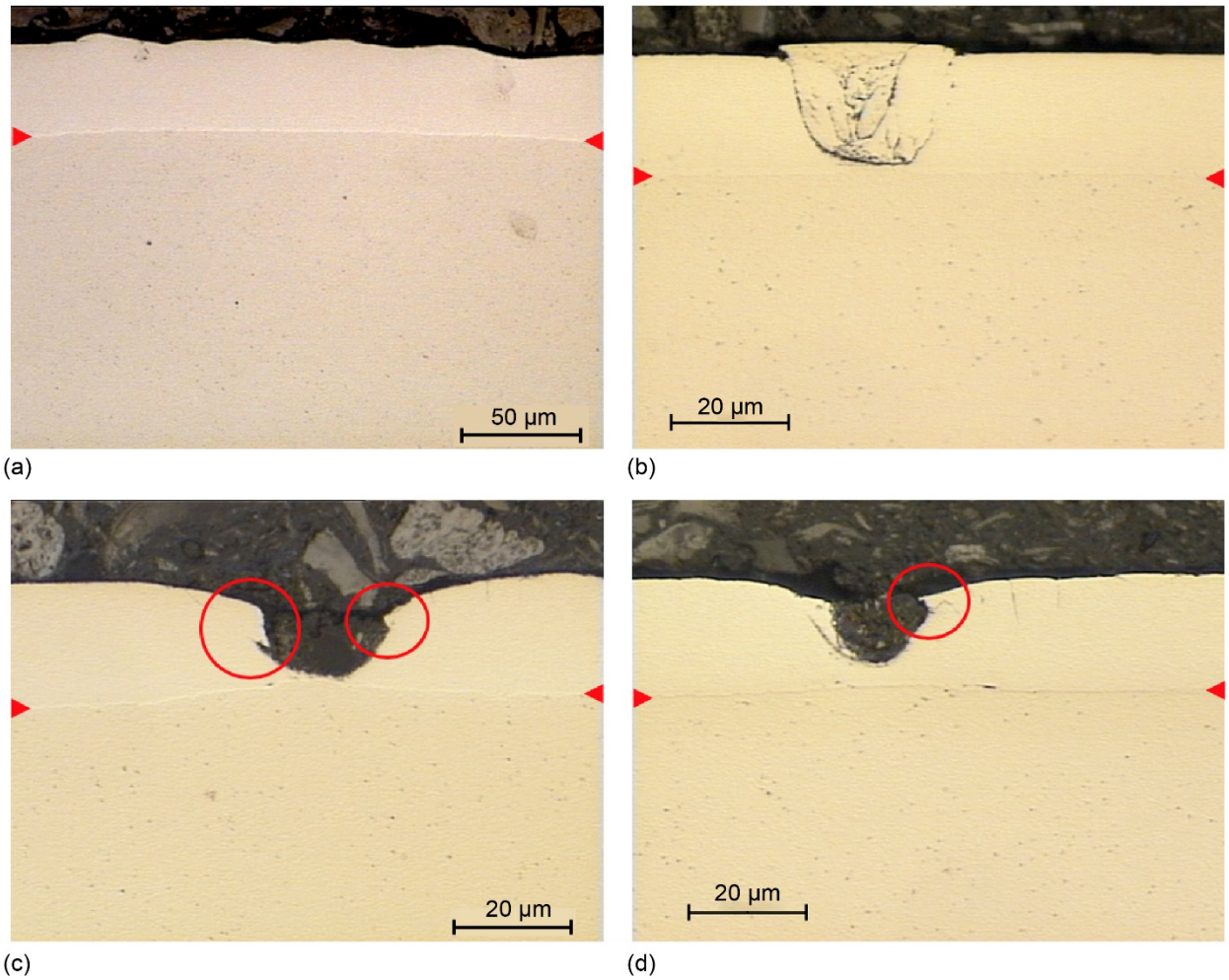

Figure 5.—Optical images of various coatings showing the effect of shot peening. (a,b) ***Low Cr*** coatings showing a wavy surface and a flattened spit. (c,d) ***High Cr, Thin*** coating showing lost spits. Red circles indicate regions of plastic flow into the hole. Red arrowheads indicate the location of the C/S interface.

Polished cross sections of these specimens exhibited the effect of the shot peening. The ***Low Cr*** coatings showed some waviness (Figure 5(a)) as expected with the deformation shown in Figure 1(a) and (d). A flattened spit is clearly shown in Figure 5(b). Regions with a lost spit creating a hole in the ***High Cr***, ***Thin*** coating are shown in Figure 5(c) and (d). Red circles indicate regions of plastic flow into the hole. This plastic deformation into the hole is believed to cause the smaller "holes" at the bottom of the dimples (Figure 2(a) and (b)).

LCF Testing After Shot Peening

After shot peening and the low PO_2 anneal, two specimens with each coating, as well as two uncoated specimens, were LCF tested. In each case, the shot peening improved the LCF life of the coated specimens, but there was no change in LCF life for the uncoated specimens (Figure 6). The blue arrows indicate the change in LCF life before and after shot peening (open and filled symbols, respectively). It should be pointed out that the baseline as-coated+low PO_2 anneal (open symbols) were mainly with the LSHR disk composition. For the ***Low Cr***, ***Thin*** coating, two specimens of both the LSHR and ME3 alloys were coated and tested (Figure 6, red, open diamonds) (Ref. 1). The overlap in the LCF lives for these compositionally-similar disk alloys, under the current LCF test conditions, suggests that the LCF lives of

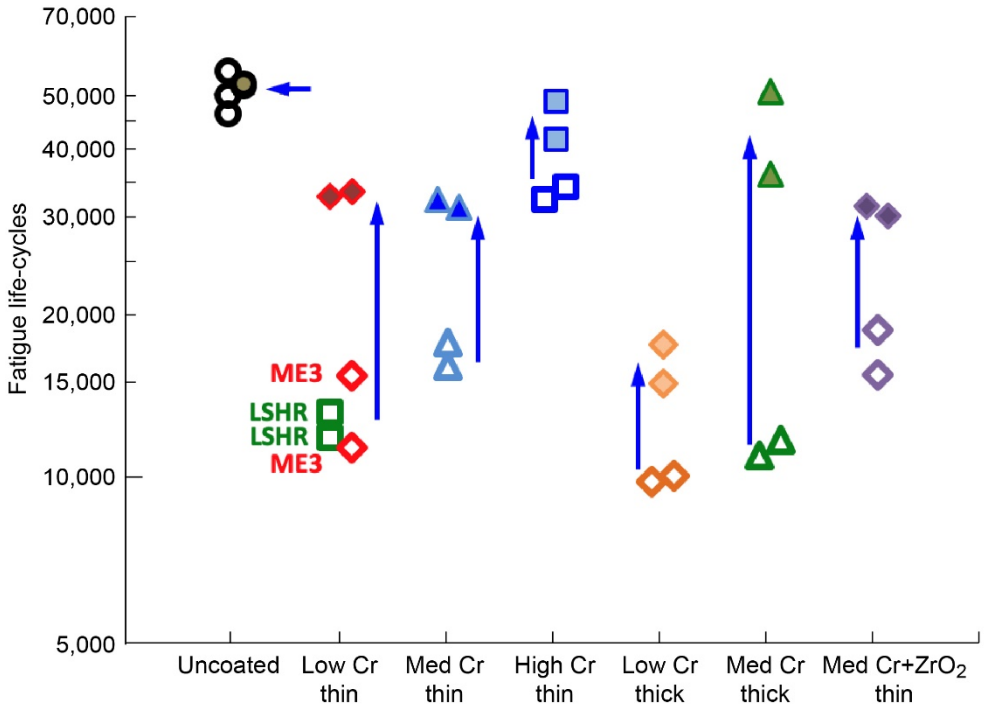

Figure 6.—LCF life before (open symbols) and after shot peening (filled symbols). All samples except the uncoated LSHR bars (open circles), also received the low PO_2 diffusion anneal prior to testing. Blue arrows indicate the change in LCF life before and after shot peening. All shot peened bars (coated and uncoated) are of the ME3 alloy. All other bars are of the LSHR alloy except for the ***Low Cr, Thin*** coated bars where both LSHR and ME3 were tested, as indicated. The results for uncoated bars are shown to the left. Note the logarithmic scale.

the two alloys are similar and the comparisons with the other coatings are valid. In addition, it should also be noted that the uncoated, unpeened specimens (open circles) did not receive the low PO_2 diffusion anneal whereas all other specimens shown in Figure 6 received this anneal. The individual LCF lives for each of the specimens shown in Figure 6, as well as the specimens from Reference 1, are tabulated in Appendix A. This appendix also shows the total time of the LCF test in hours (i.e., the exposure time at 760 °C), and the total exposure time at 760 °C including the 8 h low PO_2 anneal.

After LCF testing, the fracture surfaces of the specimens were examined to determine initiation sites and the likely cause for the initiation of the primary crack responsible for failure. The location of the primary crack initiation site was often easily observed visually as shown in Figure 7(a). EDS spectra of the fractured coating shows a Cr-rich outer layer, likely Cr_2O_3, but also with significant Al (likely Al_2O_3) (Figure 7(c) and (d)). EDS spectra at the surface in other regions showed even higher Al concentrations although no Al is apparent in the center of the coating (Figure 7(c) and (e)). Since the coating contains no Al, the only source of Al is diffusion from the substrate. The LCF life for this ***Low Cr***, ***Thin*** coated specimen was 32,650 cycles which translates to 27.2 h of exposure time at 760 °C during the LCF test. The addition of the 8 h anneal at 760 °C yields a total exposure time at 760 °C of 35.2 h (Appendix). Hence, it appears that Al from the substrate, at a level of only 3.2 wt%, was able to diffuse through the thin coating to be selectively oxidized on the surface. This 760 °C exposure time of 35.2 h was near the midpoint of the exposure times for these coated specimens which ranged from 20.4 to 50.2 h (Appendix). Comparison of the EDS spectra for the substrate near (Figure 7(c) and (f) and far (Figure 7(g)) from the coating shows a higher Cr concentration near the coating due to Cr diffusion from the coating into the substrate.

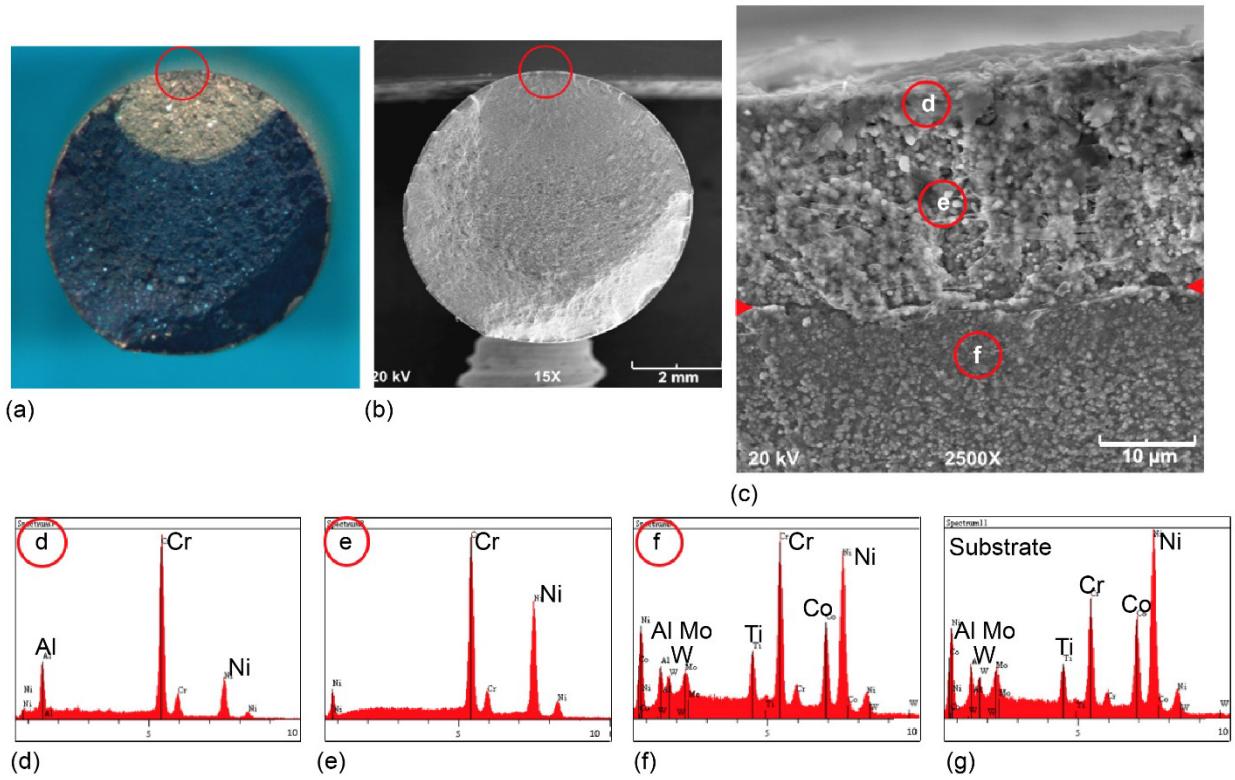

Figure 7.—(a) Optical and (b) BSE images of the fracture surface of one of the LCF bars with the ***Low Cr, Thin*** coating. (c) Magnified SE image of the coating showing locations of the three EDS spectra shown in (d-f). (g) is the EDS spectra of the substrate away from the coating. Red arrowheads indicate the location of the C/S interface. Note the Al in the spectra near the surface (d).

After examining the fracture surface, the specimen was rotated and the coated surface of the specimen was also examined in the region where the primary failure crack initiated. SEM images of the sides of the coated specimens for each of the coatings are shown in Figure 8. As with the unpeened coatings examined in Reference 1, the ***High Cr***, ***Thin*** coating showed the most fatigue cracks in the coating (Figure 8(c)). Fewer cracks are seen in the ***Med Cr***, ***Thin*** coating (Figure 8(b)) than in the ***Low Cr***, ***Thin*** coating (Figure 8(a)), unlike that in Reference 1. Few cracks are shown in the ***Low Cr***, ***Thick*** coating (Figure 8(d)) and the ***Med Cr+ZrO$_2$***, ***Thin*** coating (Figure 8(f)). Large deep cracks in the ***Med Cr***, ***Thick*** coating again show that this coating has become largely detached from the substrate as shown in the image inset (Figure 8(e)).

Frequent instances of cracking at flattened spits are highlighted in the SE and BSE images in Figure 9(a) and (b). The BSE image clearly shows fatigue cracks associated with the flattened spits indicating a failure of shot peening to weld or bond the spit to the coating. A magnified view of a fatigue crack passing around a flattened spit highlights the poor bond remaining between the spit and coating after peening (Figure 9(c)). Chromium-rich oxide nodules are also apparent on the surface of the coating (Figure 9(c)). In the bottom right corner of Figure 9(a) and (b) is a hole caused by the loss of a spit. As with the flattened spits, the hole is intersected by a fatigue crack. From an examination of the fracture surfaces, it was apparent that the spits, although flattened, continued to act as crack initiation sites, as shown by the presence of a flattened spit at the primary crack initiation site in Figure 10. Examination of the surface of other coated specimens showed that most fatigue cracks were associated with either a flattened spit or a hole. The exceptions were the ***Med Cr***, ***Thick*** coating in which the coating delaminated from the substrate (Figure 8(e)) and the ***Med Cr+ZrO$_2$*** coating in which the thin ZrO_2 outer layer

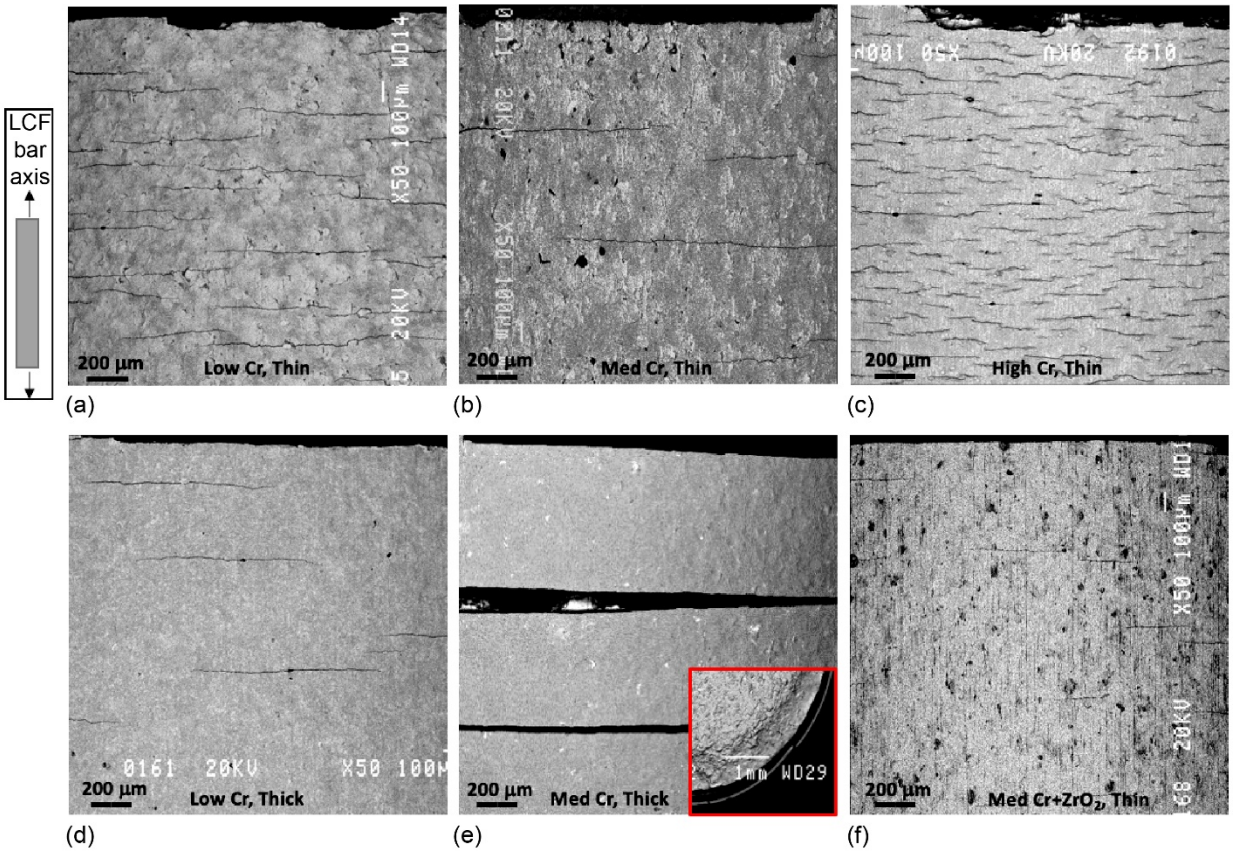

Figure 8.—BSE images of the sides of the coated bars after fatigue testing showing varying amounts of fatigue cracks. Fracture surfaces are at the top. Inset in (e) shows the significant delamination of the ***Med Cr, Thick*** coating as viewed on the fracture surface.

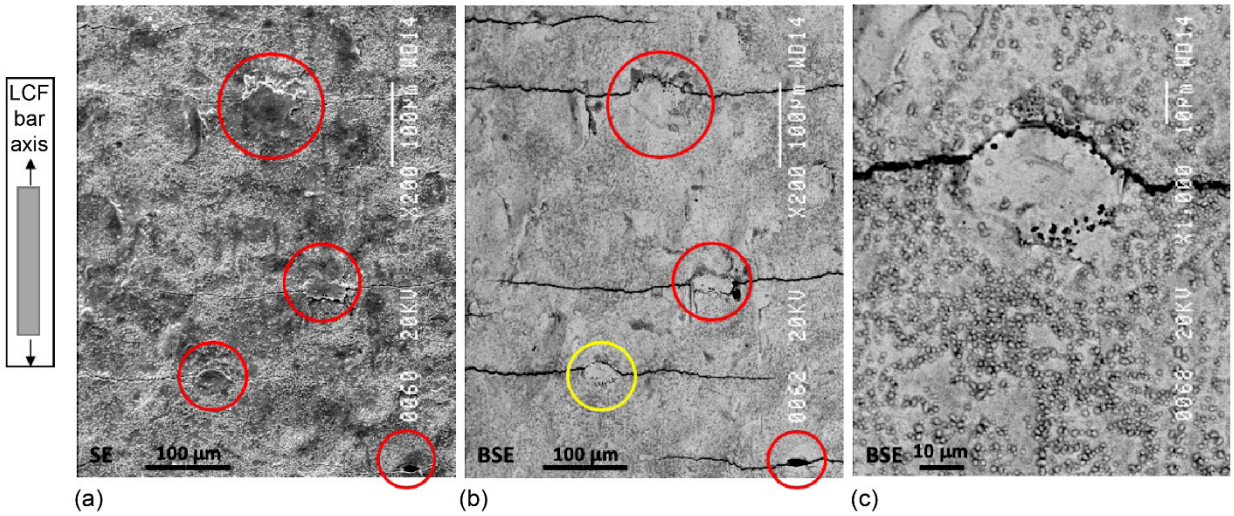

Figure 9.—(a) SE and (b,c) BSE images of flattened spits on the sides of the of the ***Low Cr, Thin*** coating. A hole from a missing spit appears in the lower right corner of (a,b) intersected by a fatigue crack. (c) is a magnified view of the yellow highlighted spit in (b). Red circles indicate the spits and hole.

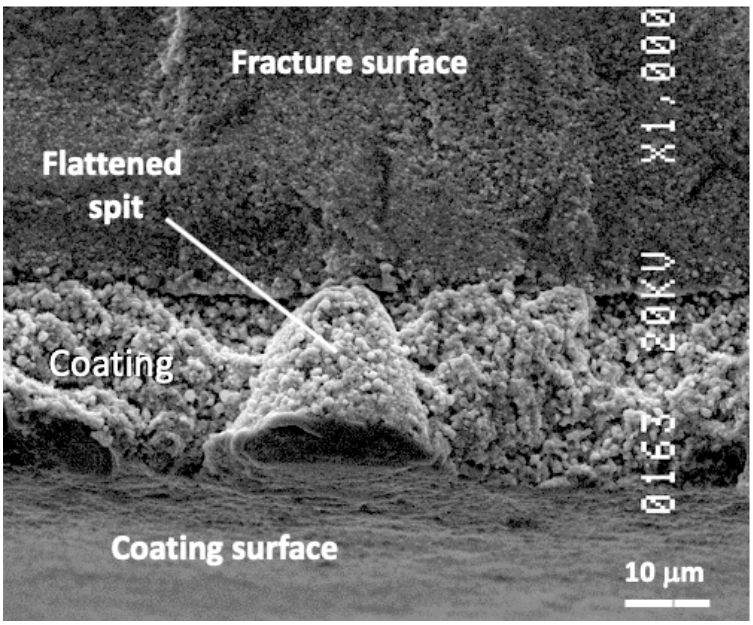

Figure 10.—SE image of the primary crack initiation site at the edge of the fracture surface of the ***Low Cr, Thin*** coating showing a clear image of a flattened spit.

appeared to have less spits, similar to what was observed in Reference 1. Lastly, the dented and dimpled surface of an uncoated specimen is shown in Figure 11. EDS analysis of the surface showed spectra similar to that of the substrate (Figure 7(g)) but with enriched concentrations of Cr and Ti and a slight enrichment of Al, as expected with the oxygen reactivity of these elements (Refs. 18 and 19). As with the unpeened specimen in Reference 1, fatigue cracks in the uncoated specimen were significantly smaller and less in number than those in the coated specimens (compare Figure 8 and Figure 11(c)).

Additional LCF specimens (coated and uncoated), as well as coated characterization pins, were oxidized for 500 h in static lab air. Typical oxide morphologies, including a flattened spit, on the surface of the ***Low Cr*** coating, are shown in Figure 12(a) and (b). EDS analysis of the surface oxides showed Cr-rich scales, likely Cr_2O_3 (Figure 12(c)). Lighter regions in the BSE images (Figure 12(b) and (f)), were still Cr-rich, but contained a slightly higher fraction of Ni (Figure 12(f)) suggesting either some $NiCr_2O_4$ spinel formation, or a thinner oxide scale allowing the Ni in the coating to be detected. The oxide on the ***Med Cr*** coating appeared more uniform with a higher fraction of the high-Cr oxide (Figure 12(d) and (e)). EDS of the brighter and darker scales were similar to those for the ***Low Cr*** coating (Figure 12(c) and (f)). The surface oxides on the ***High Cr*** coating appeared more uniform and dense (Figure 13(a) and (b)) and nearly all Cr (likely Cr_2O_3) except for a significant enrichment of Ti (Figure 13(c)). The only source for the Ti was again the substrate with a Ti concentration of 3.6 wt%. It is interesting that Al was detected with the Cr_2O_3 at relatively short exposures (~35 h) (Figure 7(c) and (d)), but Ti was detected after longer exposures (500 h). An EDS spectra measured at the bottom of a hole showed a higher Ti concentration, likely due to the proximity of the substrate. The surface of the ***Med Cr+ZrO₂*** coating after the oxidation exposure is shown in Figure 14. The longitudinal gaps and coating texture along the load axis of the specimen are still evident. An EDS spectra of the surface shows the Zr of the outer ZrO_2 layer but with significant levels of Cr and lower levels of Ni. The oxygen peak was negligible due to low energy x-ray detection. As will be shown in the following section, the high Cr peak is due to Cr_2O_3 formation below the outer ZrO_2 layer.

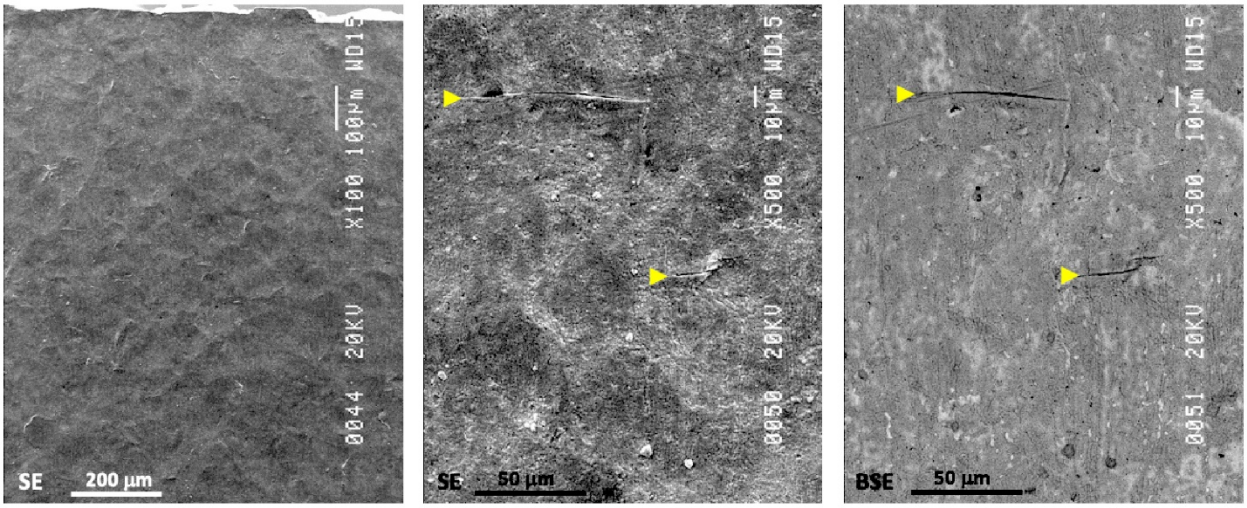

(a) (b) (c)

Figure 11.—(a,b) SE and (c) BSE images of the surface of an uncoated bar after LCF testing. Two fatigue cracks are highlighted with yellow arrowheads in (c). Fracture surface is to the top of the images (specimen loading axis is vertical).

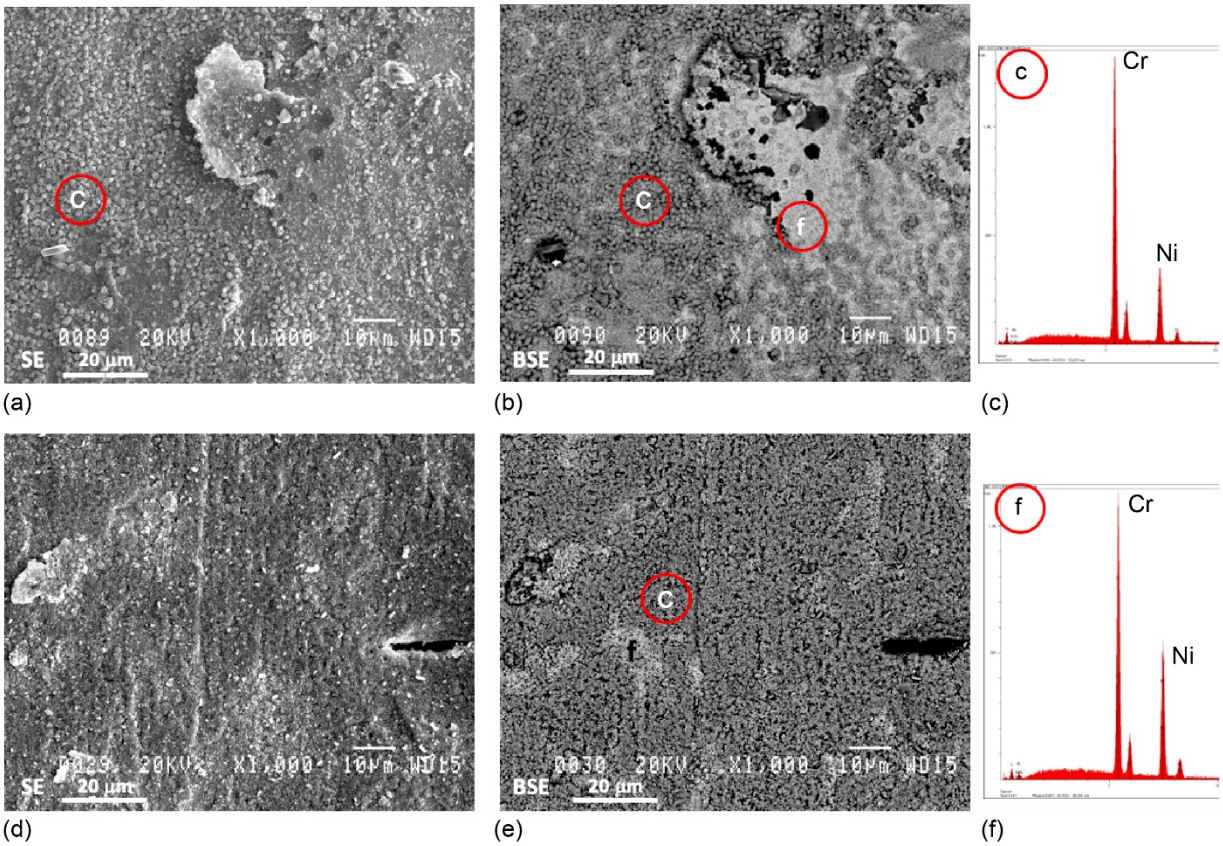

(a) (b) (c)

(d) (e) (f)

Figure 12.—(a,d) SE and (b,e) BSE images of the surface of the (a,b) ***Low Cr*** coating and (d,e) ***Med Cr*** coating after 500 h of oxidation in air at 760 °C. A flattened spit is evident in both (a,d). EDS spectra of the darker and lighter oxide shown in the BSE images (b,e) is shown in (c,f).

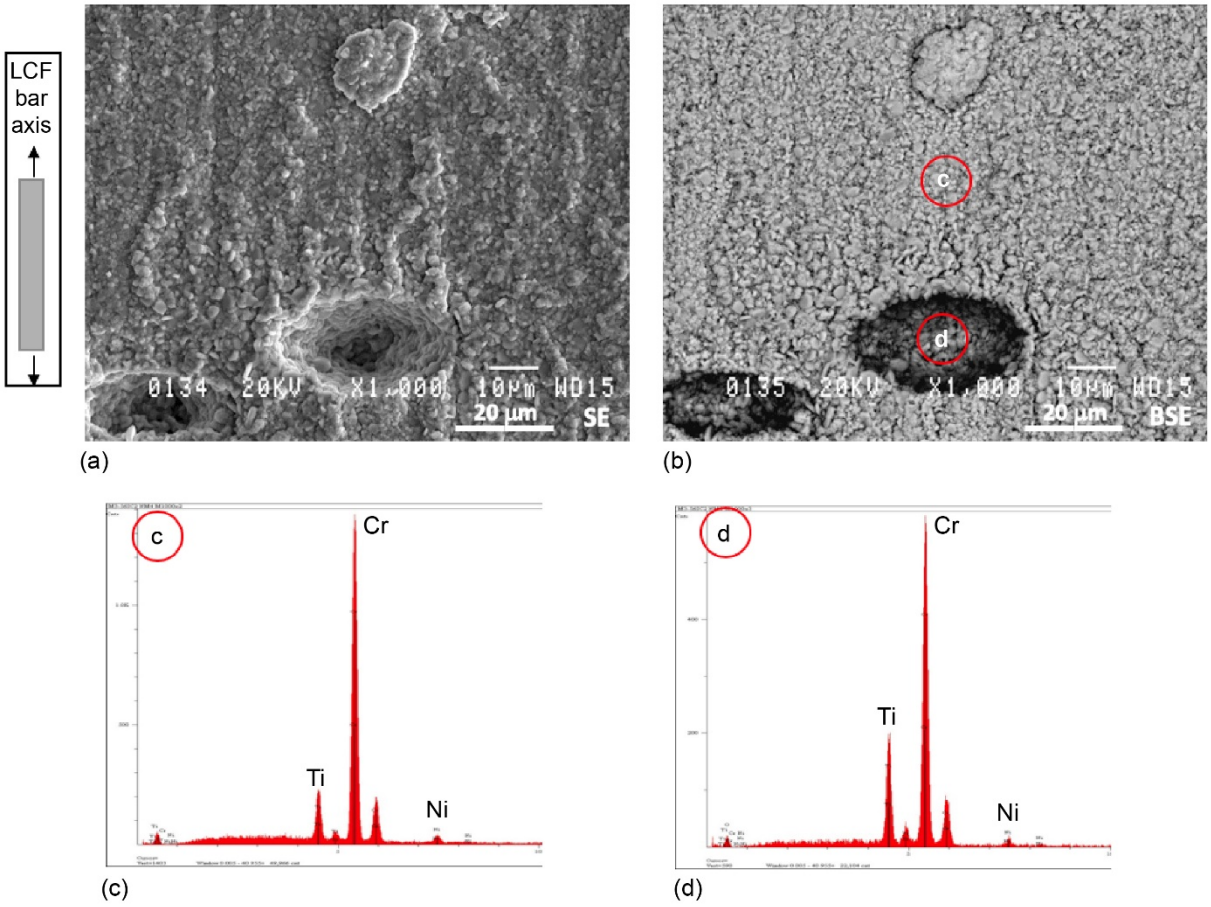

Figure 13.—(a) SE and (b) BSE images of the surface of the ***High Cr*** coating after 500 h of oxidation in air at 760 °C. A flattened spit is evident at the top of the image and two holes from lost spits are shown at the bottom. EDS spectra of the surface oxide and the bottom of the hole are shown in (c,d).

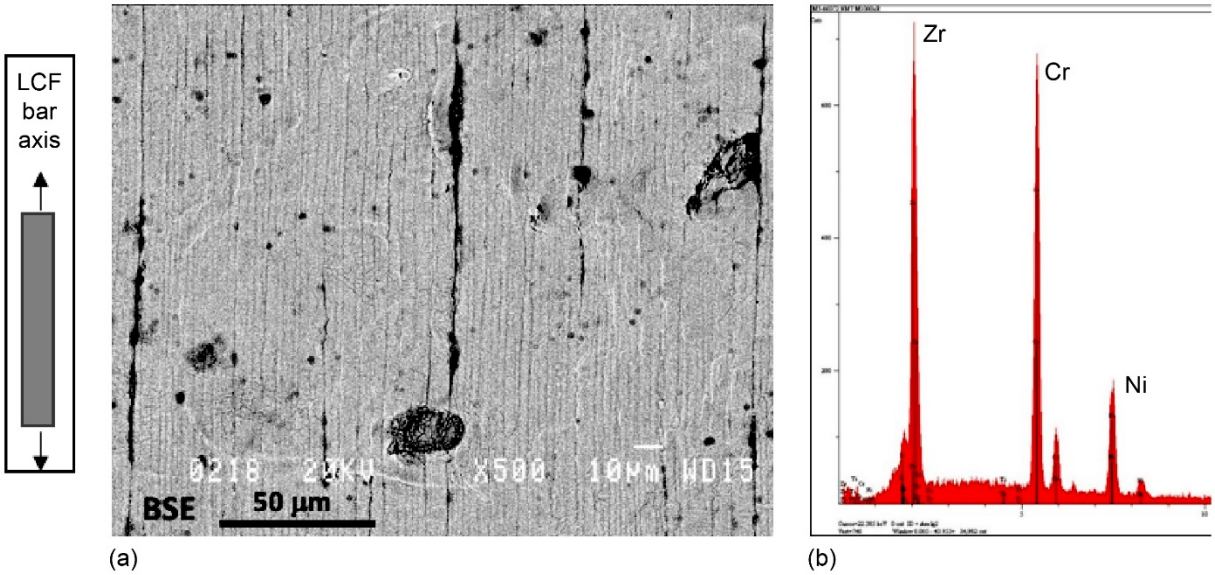

Figure 14.—(a) BSE image of the surface of the ***Med Cr+ZrO$_2$*** coating after 500 h of oxidation in air at 760 °C. (b) EDS of the surface.

Some of the coated and oxidized characterization pins were sectioned, mounted and polished. Images of the ***Low Cr***, ***Thin*** and ***Low Cr***, ***Thick*** coatings are shown in Figure 15. It is interesting that Kirkendall-pores have formed at the surface, likely due to the diffusional transport of Cr to the surface where it was selectively oxidized. Some of the pores are open to the surface and contained oxide. In other regions, very fine, near-surface pores were evident (Figure 15(c)). The surface oxide was Cr-rich with some Ni, similar to what was observed previously on the surface of this coating (Figure 12(a) to (c) and (f)). What is likely a flattened spit (Figure 15(e)) has the appearance of a "lap" (folded over metal) observed on shot peened surfaces (Ref. 4). A closer examination of the coating microstructures showed that there was a thin, recrystallized layer below the original coating/substrate (C/S) interface of approximately 2 to 3 μm thick. The ***Med Cr***, ***Thin*** coating exhibited a similar microstructure to the ***Low Cr*** coating (Figure 16). Small Kirkendall pores were evident below the Cr_2O_3 scale and a thin, recrystallized layer existed below the coating. However, the α-Cr phase was evident throughout the coating with some larger particles (Figure 16(a) and (b)). The random, large α-Cr particles dispersed in the coating with smaller particles has been observed before and is unexplained (Ref. 20). A spit with oxidized interfaces is clear in Figure 16(c). The microstructure of the ***Med Cr***, ***Thick*** coating looked very similar to the ***Med Cr***, ***Thin*** coating. Small Kirkendall pores have been observed previously following oxidation at a similar

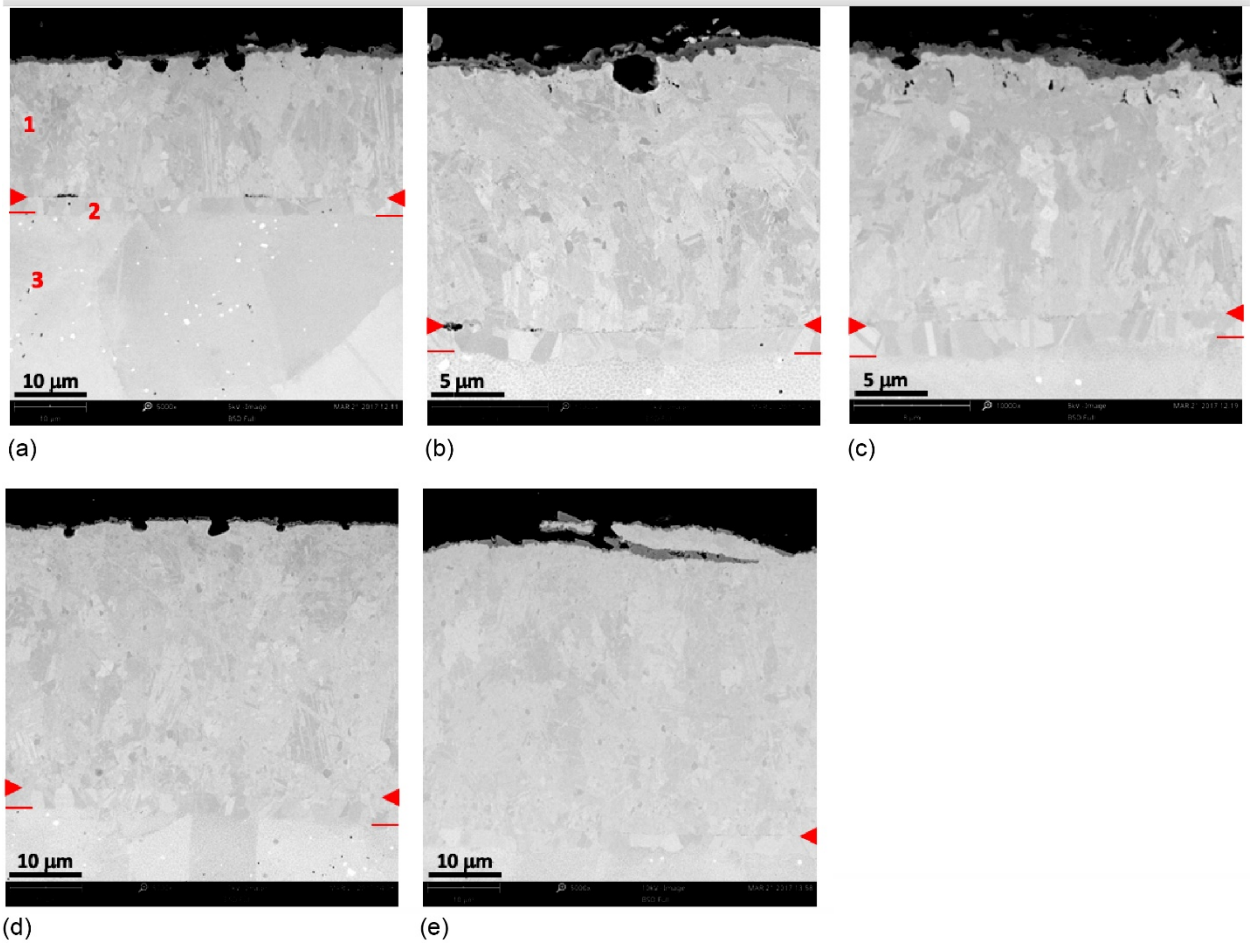

Figure 15.—(a-c) BSE images of polished cross-sections of the ***Low Cr, Thin*** coating and (d,e) ***Low Cr, Thick*** coating after 500 h of oxidation in air at 760 °C. Red arrowheads indicate the original C/S interface. The short red line below the red arrowhead indicates the depth of the recrystallized layer. The numbers 1,2,3 refer to the coating, recrystallized layer and disk alloy, respectively in (a).

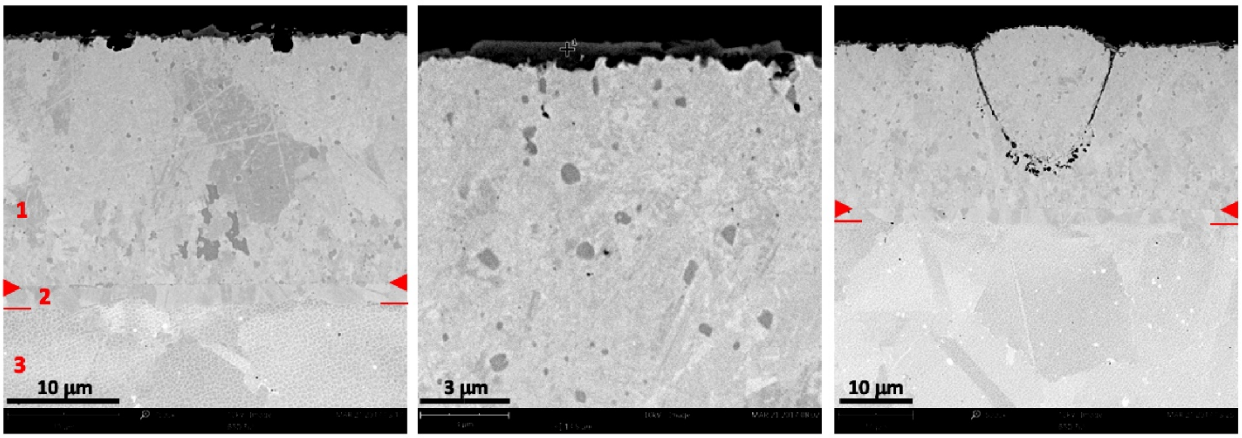

(a) (b) (c)

Figure 16.—(a-c) BSE images of polished cross-sections of the ***Med Cr, Thin*** coating after 500 h of oxidation in air at 760 °C. Red arrowheads indicate the original C/S interface. The short red line below the red arrowhead indicates the depth of the recrystallized layer. The numbers 1,2,3 refer to the coating, recrystallized layer and disk alloy, respectively in (a).

temperature resulting in the formation of a primarily Cr_2O_3 scale on the surface of an uncoated disk alloy (Ref. 21). The pores form due to the unequal diffusional flux of Cr to the surface. A thin layer of recrystallized grains below the oxide scale were also observed in this earlier study (Ref. 21).

There were significant differences in the microstructure of the ***High Cr***, ***Thin*** coating, as shown in Figure 17. Some larger, near-surface Kirkendall pores were still evident, but there was a distinct, uniform layer of what appeared to be fine porosity approximately 5 to 6 µm thick. The amount and size of α-Cr particles were reduced in this near-surface region. Most of the α-Cr particles had also receded from the C/S interface see blue arrows) to a position nearly at the center of the coating due to diffusion of Cr into the substrate, although some fine, unidentified particles were observed in this largely α-depleted layer (Figure 17(e)). It is possible that these fine particles were α-Cr but were too small for definitive EDS analysis. Some large particles of α-Cr had not fully dissolved, likely due to their size, as shown in Figure 17(c). It appears that the recrystallized layer below the C/S interface is slightly thicker (3 to 4 µm thick) than for the lower-Cr coatings, perhaps due to a higher amount of Cr diffusion into the substrate. Oxidation of a large, partially filled hole was also evident (Figure 17(f)). A dimple in the surface above this hole is also obvious.

A magnified view of the outer region of this coating is shown in Figure 18(a). The fine Kirkendall pores, presumably formed by the unequal diffusional flux of Cr to the surface, appear elongated along grain boundaries. It is not known if there is any oxidation (e.g., Al_2O_3) within the pores. A closer examination of this porous subscale region shows that small second-phase particles still remain in this near-surface layer. It is assumed that these particles are simply smaller particles of α-Cr. EDS spectra at four locations in the outer half of the coating are shown in Figure 18. As noted previously in Figure 13, the outer oxide scale is Cr-rich (presumably Cr_2O_3) but with some Ti (Figure 18(a) and (b)). However, the oxide growth into the coating has a much higher concentration of Ti along with some Al and Ta (Figure 18(a) and (c)). An EDS spectra within the coating shows many of the substrate elements (Co, Al, Ta, Mo) which have diffused into the coating but only a small peak for Ti (Figure 18(a) and (d)). Curiously, an EDS spectra taken below the porous sub-scale region shows the substrate elements but without Ti (Figure 18(a) and (e)). Apparently Ti is rapidly diffusing to the surface and being selectively oxidized to result in a low concentration in the coating. Because the ***Med Cr***, ***Thick*** coating was easily detached from the substrate, it will not be discussed in this section.

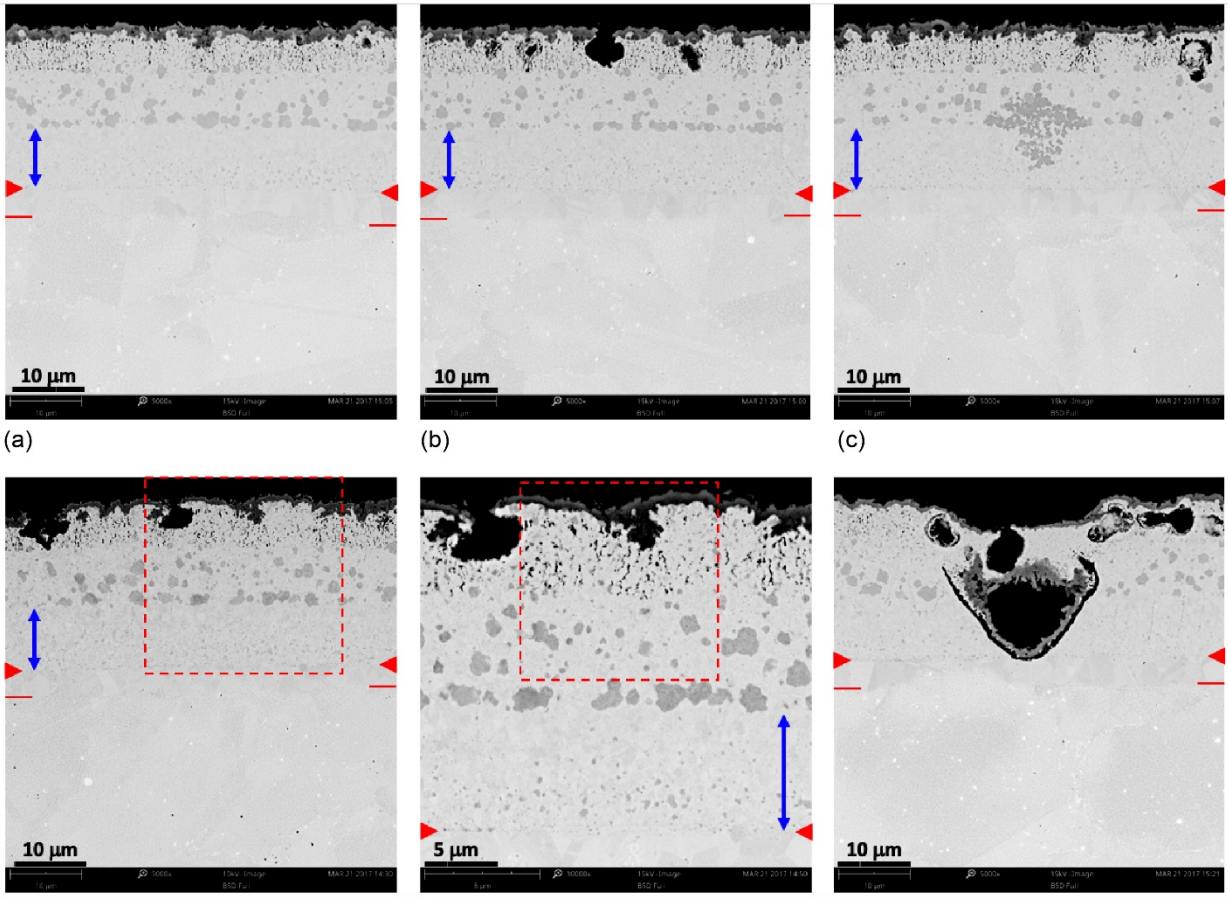

Figure 17.—BSE images of polished cross-sections of the ***High Cr, Thin*** coating after 500 h of oxidation in air at 760 °C. Red arrowheads indicate the original C/S interface. The short red line below the red arrowhead indicates the depth of the recrystallized layer. The dashed box in (d) is magnified in (e). The blue arrows indicates the α-depleted region containing fine, unidentified particles.

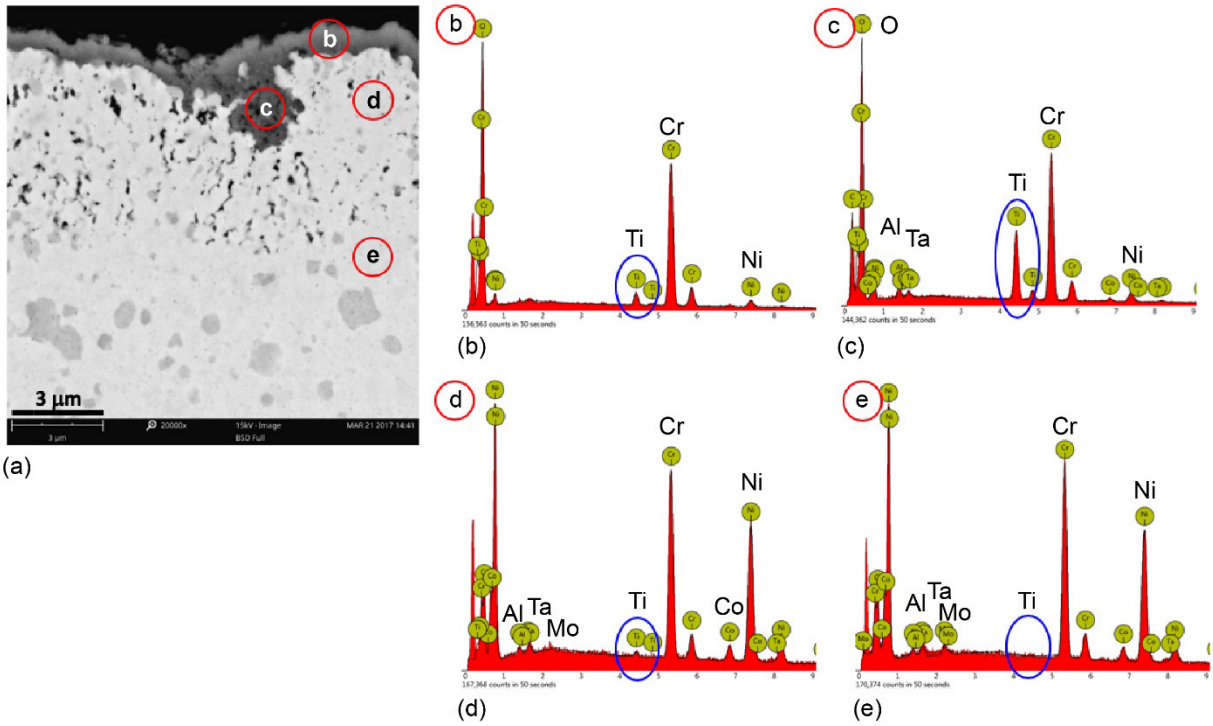

Figure 18.—(a) BSE image of the dashed box shown in Figure 17(e). (b-e) EDS spectra of the locations labeled b-e in (a).

The ***Med Cr+ ZrO_2***, ***Thin*** coating after the 500 h oxidation exposure is shown in Figure 19. Below the outer Zr-rich oxide layer, a Cr-rich oxide formed under the ZrO_2 layer (dark layer below the bright ZrO_2 outer layer in Figure 19(c)), consistent with the Zr, Cr oxides detected previously by EDS from the outer surface (Figure 14). A dimple in the surface, likely over a partially-filled hole, is shown in Figure 19(d). Oxidation along the original spit or hole boundary is evident. A flattened spit is shown in Figure 19(e). A closer examination showed that ZrO_2 still remained on some outer portions of this flattened spit although with obvious cracks in the layer.

After the 500 h oxidation exposure, the specimens were exposed to a hot corrosion exposure for 50 h at 760 °C as described in the **Experimental Procedures** section. Corrosion morphologies for the five ***Low***, ***Med***, and ***High Cr*** coatings were similar. Typical surface morphologies after the hot corrosion exposure, and prior to ultrasonic washing, are shown for three of the coatings in Figure 20. All surfaces contained large regions of nearly pure Na_2SO_4 (dark, cracked regions in Figure 20(a) to (c) and associated EDS spectra in Figure 20(d)). Brighter oxide structures (see oxide labelled **e** in Figure 20(a) and (b) and EDS spectra in Figure 20(e)) were Mg and Cr-rich oxides, presumably MgO and Cr_2O_3. Bright regions in the ***Med Cr+ZrO_2*** coating (labelled **f** in Figure 20(c)) were exposed regions of the ZrO_2 layer with a large Cr enrichment (with some Ni), presumably from the Cr_2O_3 layer which formed below the ZrO_2 during the oxidation exposure (Figure 20(f)). These bright regions above the ZrO_2 were unique to the ***Med Cr+ZrO_2*** coating.

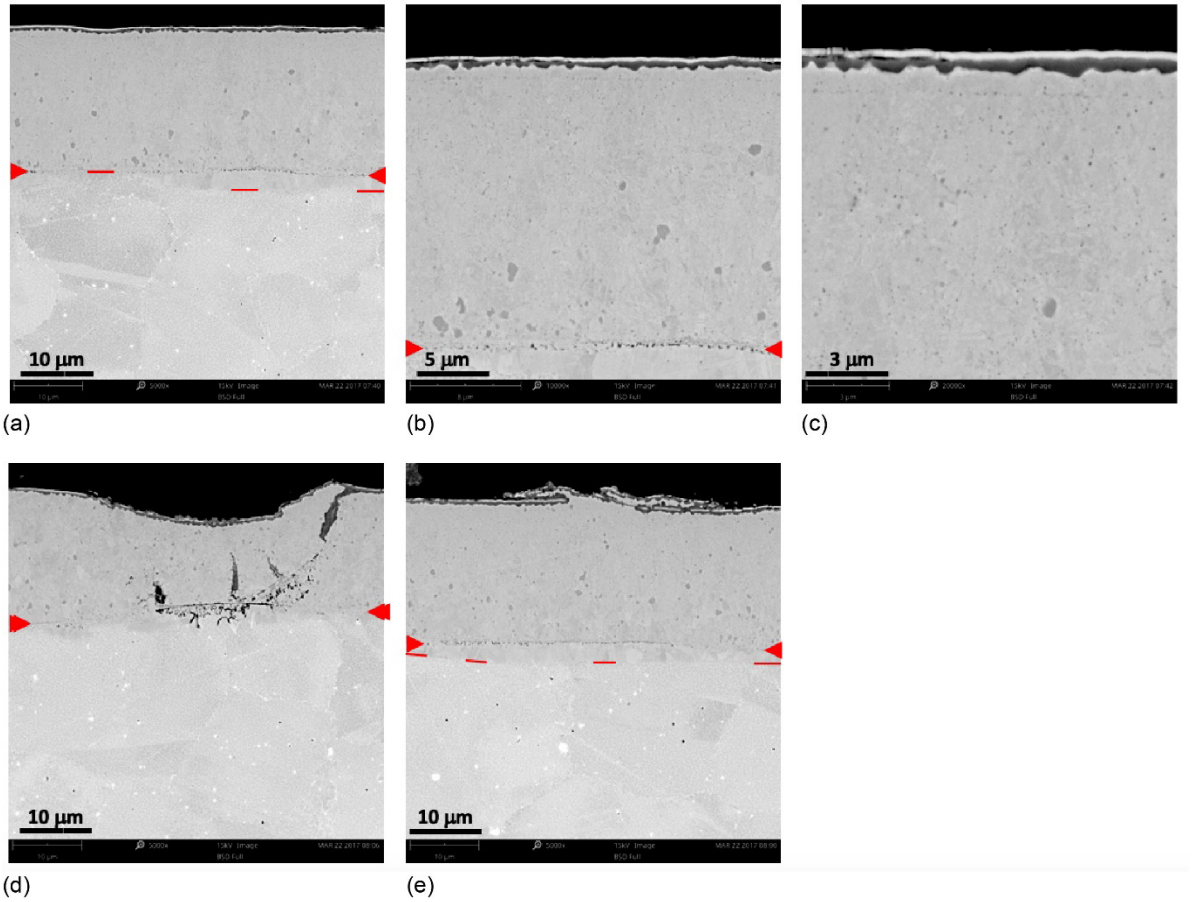

Figure 19.—BSE images of polished cross-sections of the ***Med Cr+ZrO_2***, Thin coating after 500 h of oxidation in air at 760 °C. Red arrowheads indicate the original C/S interface. The short red line below the red arrowhead indicates the depth of the recrystallized layer. The thickness of the recrystallized layer is seen to vary in (a,e).

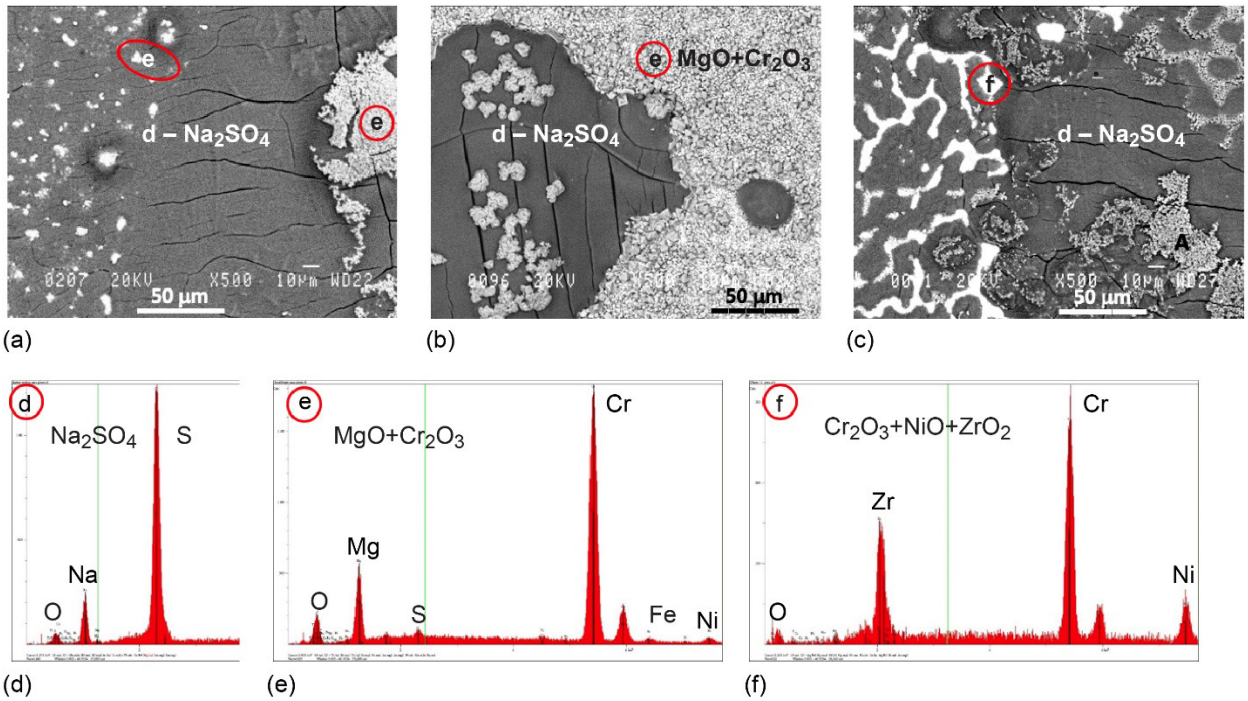

Figure 20.—BSE images of the (a) ***Low Cr, Thin***, (b) ***High Cr, Thin*** and (c) ***Med Cr+ZrO₂, Thin*** coatings after hot corrosion for 50 h at 760 °C before ultrasonic washing. (d-f) EDS spectra of Na_2SO_4 and the locations labeled (d-f) in (a-c).

After ultrasonic washing, most of the Na_2SO_4 was removed from the surface leaving adherent surface oxides with other regions showing exposed coating. It should be emphasized that no corrosion pits were observed in any of the coated specimens. A typical surface morphology for the ***Low*** and ***Med Cr*** coatings is shown in Figure 21. The bright regions in Figure 21(a) and (b) show the exposed NiCr coating, identified in the EDS spectra in Figure 21(d). The Kirkendall porosity previously observed in polished cross sections is apparent on the exposed metallic surface, primarily outlining some of the grain boundaries. The dark areas (labelled **e** in Figure 21(b) and (c)) are intact oxide which appears to be primarily Cr_2O_3 with a little MgO, as indicated in the EDS spectra shown in Figure 21(e).

The oxide morphology for the ***High Cr*** coating is shown in Figure 22(a) and (b). This oxide morphology is much more varied and mixed than that shown previously for the ***Low*** and ***Med Cr*** coatings. The intermediate gray oxide is primarily Cr_2O_3 with a small amount of MgO but significant amounts of TiO_2 (Figure 22(b) and (c). The darkest oxide is Cr_2O_3 with significant amounts of MgO (Figure 22(b) and (d)). The light regions are again the exposed coating, but with noticeable amounts of Al and Ti (Figure 22(b) and (e)). The surface of the ***Med Cr+ZrO₂*** coating is shown in Figure 23(a) to (c). Although the dark oxide again appears to be Cr_2O_3+MgO, a Zr peak indicates the presence of ZrO_2 below the Cr_2O_3+MgO scale (Figure 23(c) and (e)). The light regions in the BSE image (Figure 23(c)) appear to be the original ZrO_2 layer, likely with Cr_2O_3 growing beneath it (Figure 23(c) and (d)) as suggested in the polished cross sections after oxidation alone (Figure 19). There is no exposed metal showing on the surface, only patches of the Cr_2O_3+MgO and the exposed ZrO_2. Again, no corrosion pits were observed on the surface of any of the coatings.

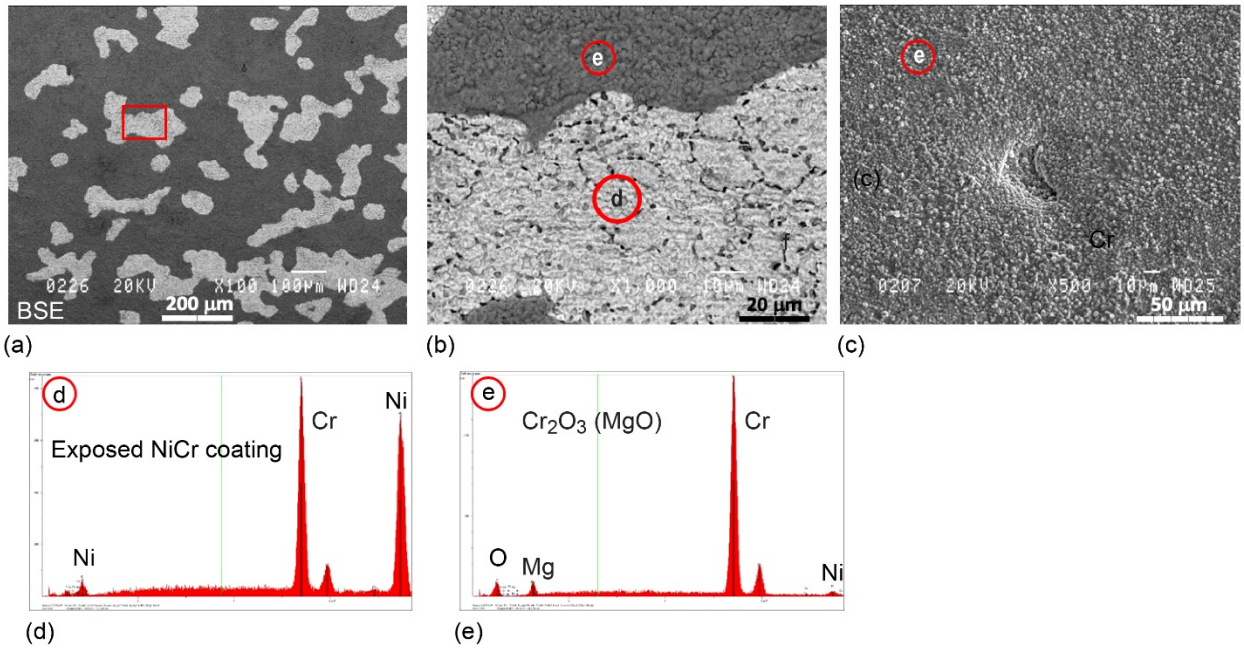

Figure 21.—BSE (a,b) and SE (c) images of the ***Med Cr, Thin*** coating after hot corrosion exposure and ultrasonic washing. (d,e) EDS spectra of exposed coating shown in (b) and retained oxide (b,c).

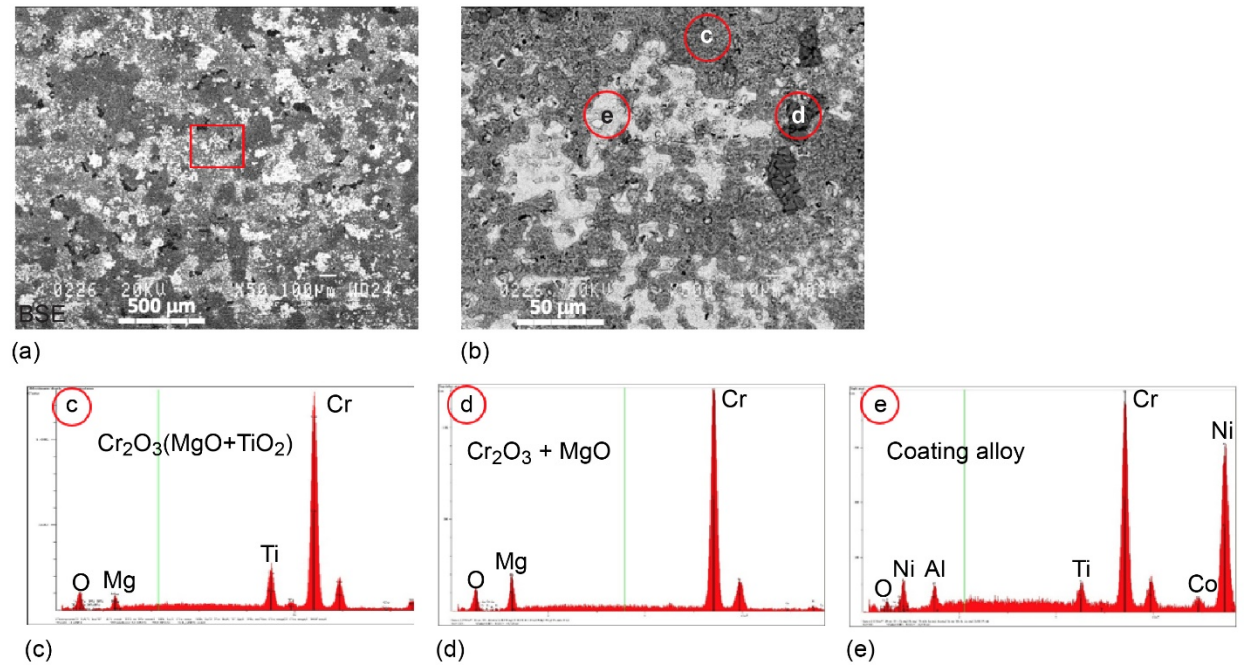

Figure 22.—(a,b) BSE images of the ***High Cr, Thin*** coating after hot corrosion exposure and ultrasonic washing. (c-e) EDS spectra of the three regions shown in (b).

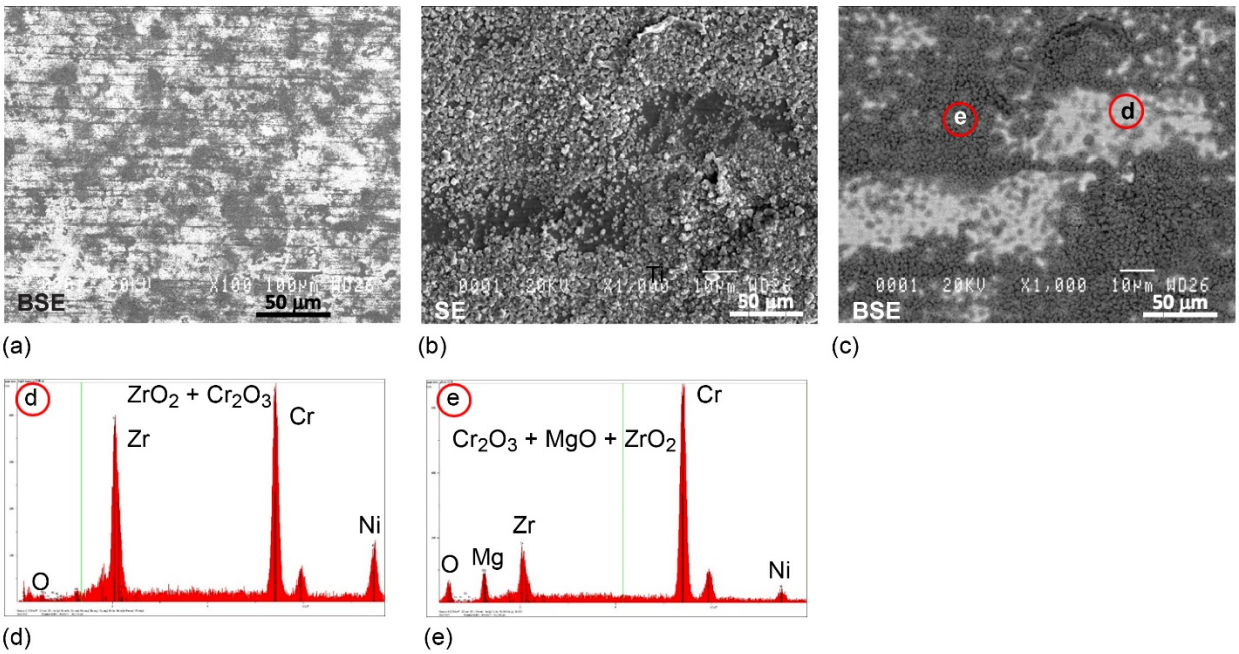

Figure 23.—(a,c) BSE and (b) SE images of the ***Med Cr+ZrO₂***, Thin coating after hot corrosion exposure and ultrasonic washing. (d,e) EDS spectra of the two regions shown in (c).

LCF Testing After Shot Peening, Oxidation, and Hot Corrosion

After the oxidation plus hot corrosion exposures and ultrasonic washing, the specimens were LCF tested at 760 °C as previously described. The LCF lives after oxidation and hot corrosion are compared with that prior to the environmental exposures in Figure 24. The red arrows indicated the change in life with the addition of the 500 h oxidation and 50 h hot corrosion exposures. As expected, most of the lives decreased with the exception of the ***Med Cr***, ***Thin*** coating which, surprisingly, showed an increase in life. The largest decrease in life was for the ***Med Cr***, ***Thick*** coating which was known to have a poor bond with the substrate. Not surprisingly, the uncoated specimens also showed a significant decrease in life with the environmental exposures. The LCF lives for each specimen after oxidation and hot corrosion exposures are also tabulated in Appendix A.

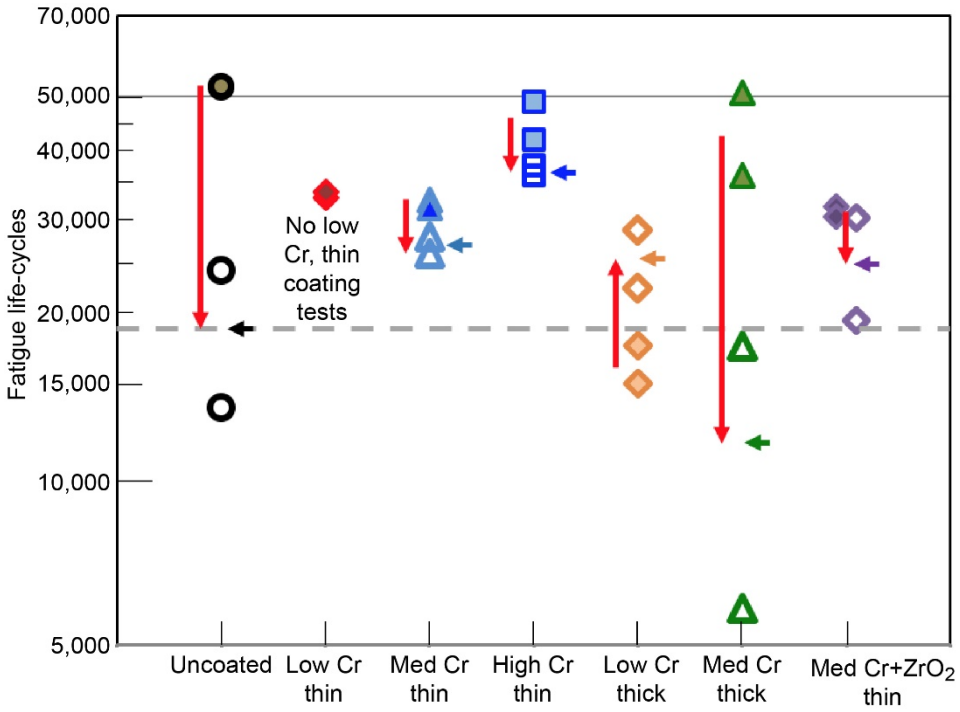

Figure 24.—LCF life for each of the coated samples showing the effect of the oxidation and hot corrosion exposures. Filled symbols show the LCF lives after shot peening and low PO_2 anneal. Open symbols show the LCF life after the oxidation and hot corrosion exposures. The red arrows indicate the approximate change in the LCF life. No samples of the ***Low Cr, Thin*** coated bars were available for testing. The results for uncoated bars are shown to the left. The dashed gray line gives the average life of the two uncoated samples. The short horizontal arrows give the average life of the two oxidized and hot corroded coated and uncoated replicate specimens. Note the logarithmic scale.

Following the LCF testing, the fracture surfaces were examined to identify the primary crack initiation site. For each of the coated and uncoated specimens, the primary crack causing failure initiated at the surface. For some of the coated specimens, a spit in the coating could be directly linked to the primary crack. After examining the fracture surface, the specimens were rotated to examine the fatigue cracks on the side of the specimen with the primary crack. The surfaces of coated specimens are shown in Figure 25. For the thin coatings (Figure 25(a) and (b)), the ***High Cr*** coating shows more fatigue cracks than the ***Med Cr*** coatings, consistent with earlier observations (Figure 8(b) and (c)). There are less cracks in the ***Med Cr***, ***Thick*** coating with the largely detached coating (Figure 25(d)), also similar to that in Figure 8(e). The fatigue cracks in the ***Med Cr+ZrO$_2$*** coating were again fine and difficult to see (Figure 25(e)), also similar to that observed previously (Figure 8(f)). At higher magnification, the cracks were highlighted with blue arrowheads to get a sense of the number of cracks. The oxide scales on the surface were the same as those identified after the hot corrosion exposure (Figure 21 to Figure 23). The additional exposure times in air at 760 °C during the LCF tests ranged from 5 h (***Med Cr***, ***Thick***) to 31 h (***High Cr***, ***Thin***). The total 760 °C exposure time for each of the specimens, including the LCF testing following oxidation and hot corrosion exposures, is given in Appendix A. The surface of an uncoated specimen following testing is shown in Figure 26. The roughly circular, bright regions are corrosion pits (Figure 26(a)). Two corrosion pits, showing obvious fatigue cracks within the pits, are highlighted by yellow circles in Figure 26(b). The primary crack initiated at the corrosion pit shown at the fracture surface in Figure 26(c).

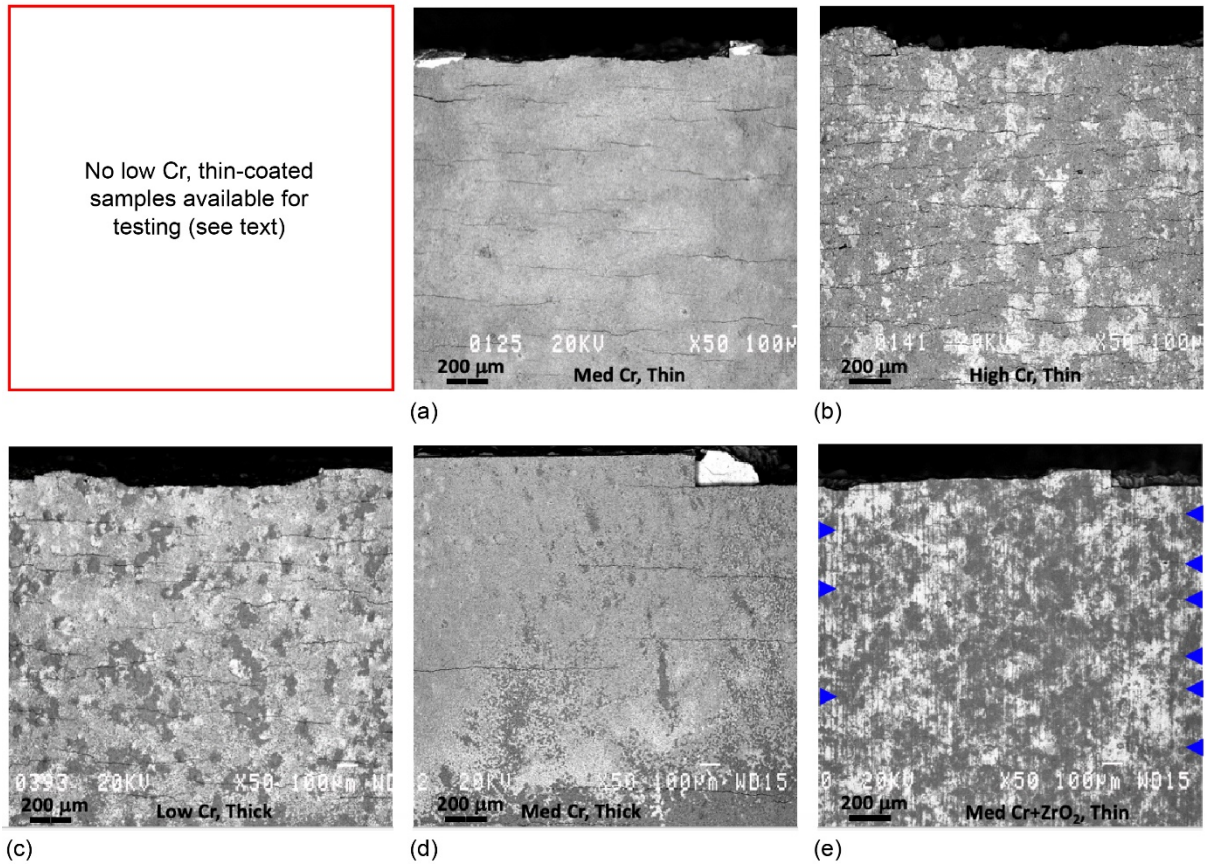

Figure 25.—BSE images of the sides of the (a) uncoated and (b-f) coated bars after oxidation and hot corrosion exposures followed by fatigue testing showing varying amounts of fatigue cracks. Fracture surfaces are at the top (specimen loading axis is vertical). No samples of the ***Low Cr, Thin*** coating were available. Blue arrowheads in (e) indicate fine cracks at the edge of the image observed at higher magnification.

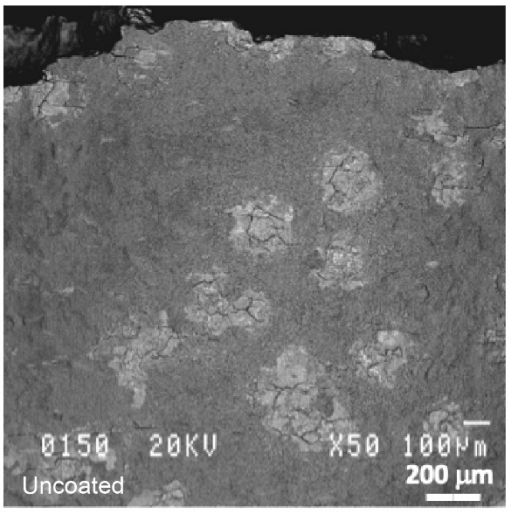

(a)

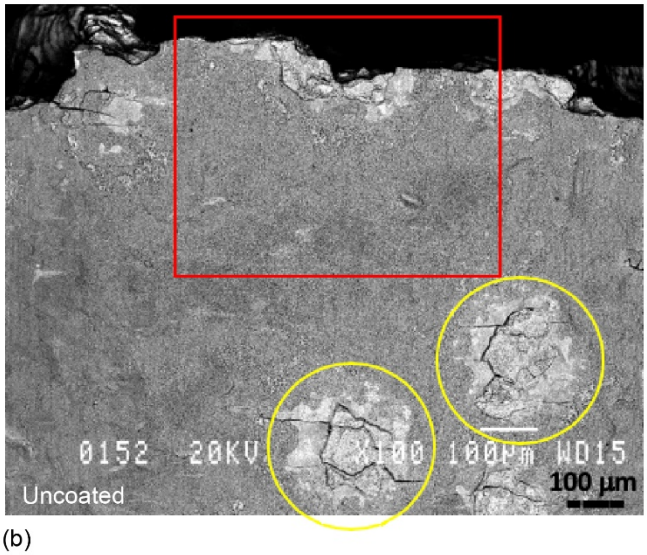

(b)

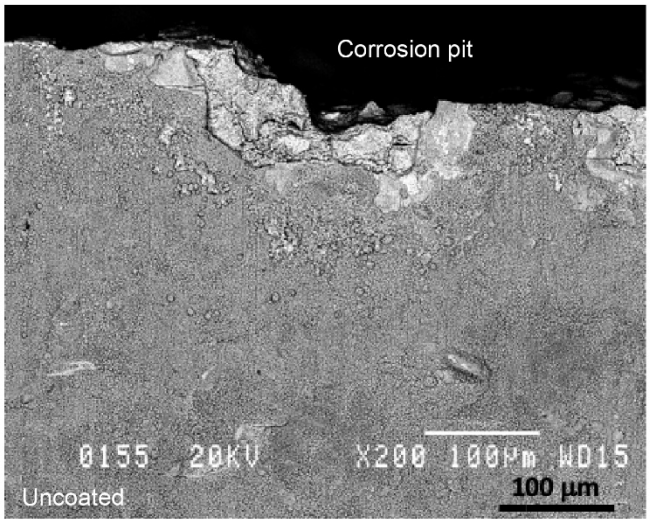

(c)

Figure 26.—(a-c) BSE images of increasing magnification of the sides of an uncoated bar after oxidation and hot corrosion exposures followed by fatigue testing (fracture surface is at the top of each image, specimen loading axis is vertical). Corrosion pits with fatigue cracks are highlighted by the yellow circles in (b). (c) is a magnified view of the red box in (b) showing the site of the primary crack initiation at a large corrosion pit.

After the SEM examination following the LCF testing, select specimens were sectioned perpendicular and parallel to the load axis and the coatings examined as described above. Coating defects, such as oxidation of spits (all specimens) and delamination of the coating (***Med Cr***, ***Thick*** coating), were as previously described. Since the fatigue cracks developed after the hot corrosion exposure, oxidation of the cracks occurred only during the fatigue testing, and as stated above, the 760 °C exposure during fatigue testing was only an additional 5 to 31 h. The main difference in the surface oxides was the addition of MgO after the hot corrosion exposure. Images of the ***Med Cr***, ***Thin*** coating are shown in Figure 27(a) to (c). The magnified views of the retained surface oxide show it is two-phase. EDS spectra (Figure 27(d) and (e)) indicate the dark phase is the Cr_2O_3+MgO, whereas the lighter phase is nearly all Cr_2O_3. Some of the α-Cr phase is also apparent in the coating (Figure 27(a) and (c)), although surprisingly, there is no significant phase depletion layer near the surface. One fatigue crack has been arrested at the substrate whereas the adjacent crack shows branching and penetration into the disk alloy (Figure 27(b)).

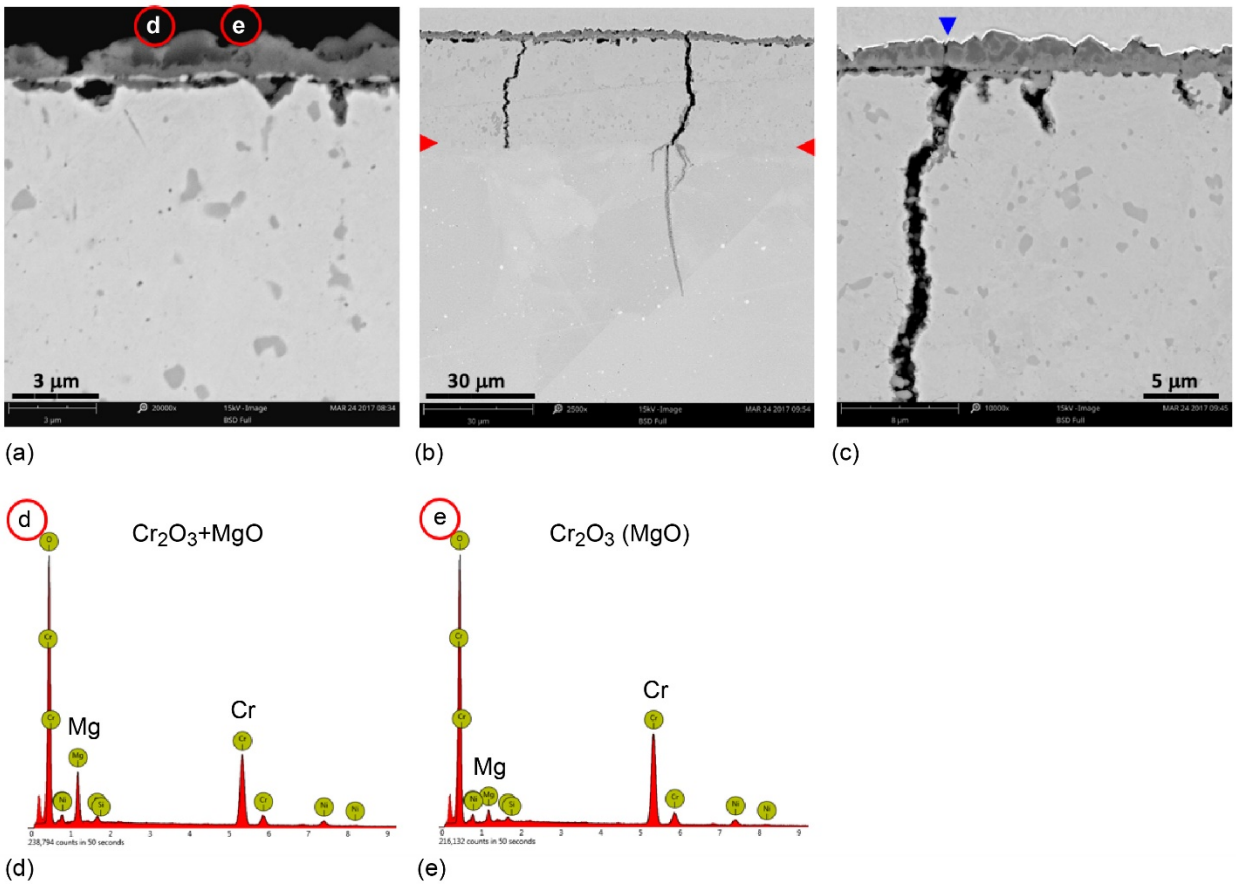

Figure 27.—(a-c) BSE images of the ***Med Cr, Thin*** coating after LCF testing following oxidation and hot corrosion exposures showing (a,c) dark and light phases in the oxide scale. Red arrowheads in (b) indicate the C/S interface. (d,e) EDS spectra of the dark and lighter phases in the scale. Mounts were polished in the direction parallel to the specimen axis to reveal fatigue cracks which formed perpendicular to the loading axis (horizontal loading axis in a-c). Blue arrowhead in (c) indicates a crack in the corrosion scale above a fatigue crack in the coating.

The microstructure of the ***High Cr***, ***Thin*** coating after oxidation, hot corrosion and fatigue testing is shown in Figure 28. The main difference in the structure of the oxide scale from what was observed after oxidation is a layering of oxide and coating alloy at the surface. Each of these oxide layers contain significant porosity. The fine particles/pores which were present below the oxide scale after oxidation are again present after hot corrosion and therefore are not likely the result of the hot corrosion exposure. That is to say, although the fine, submicron particles have the appearance of sulfides, they are believed to be the same Kirkendall pores which were present after oxidation. There is a distinct layer depleted of the α-Cr phase nearest the surface as well as on the substrate side of the coating. The EDS spectra shown in Figure 28(d) and (e) show that the lighter oxide phase is likely Cr_2O_3 while the darker phase is a mix of Cr_2O_3, MgO, TiO_2 and Al_2O_3, or mixed oxides of these components. There was no noticeable difference in the EDS spectra between points labelled **f** (in the oxide subscale) and **f'** (in the coating below the oxide subscale), but the EDS spectra in the subscale region (Figure 28(f)) gives evidence of the interdiffusion of the coating and substrate after the 550+ h of exposure at 760 °C. The oxide phases at the bottom of a hole are shown in Figure 29. The inner portion of the oxide contains significant Al (as Al_2O_3 or $CrAl_2O_4$). The higher Al content over that in the surface scale may be due to the close proximity of the bottom of the hole and the disk alloy. An examination of the fatigue cracks in the ***High Cr***, ***Thin*** coating is shown in Figure 30. It is apparent that some of the cracks penetrated as a single crack into the substrate (Figure 30(a)) whereas some of the cracks showed significant branching (Figure 30(b) and (c)). Although it cannot be stated with certainty for these two-dimensional sections, it appears that the single cracks have penetrated much deeper into the substrate whereas the branched cracks show much shallower penetration.

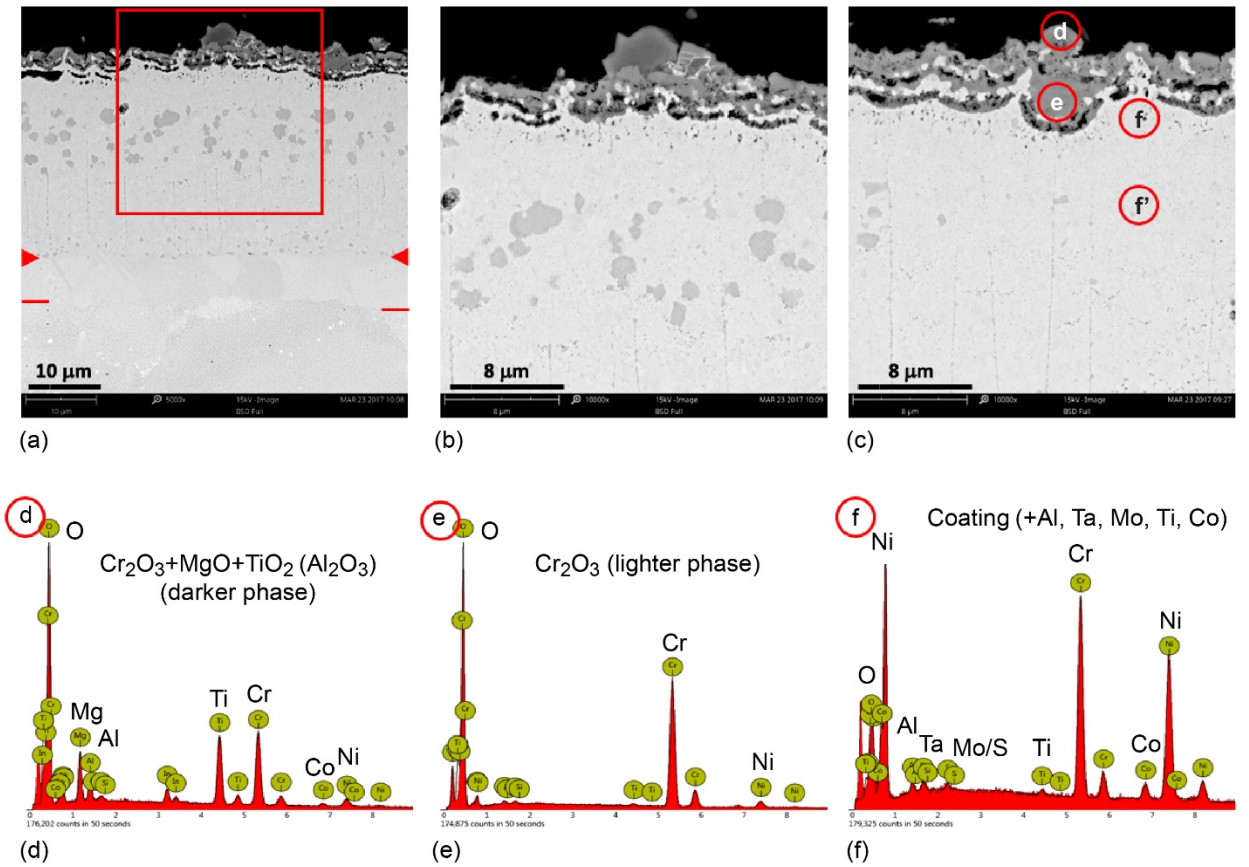

Figure 28.—(a-c) BSE images of the ***High Cr, Thin*** coating after LCF testing following oxidation and hot corrosion exposures showing multilayers in the corrosion scale (d-f) EDS spectra of the area indicated in (c). Spectra at areas (f) and (f') were nearly identical. Mounts were polished perpendicular to the specimen axis.

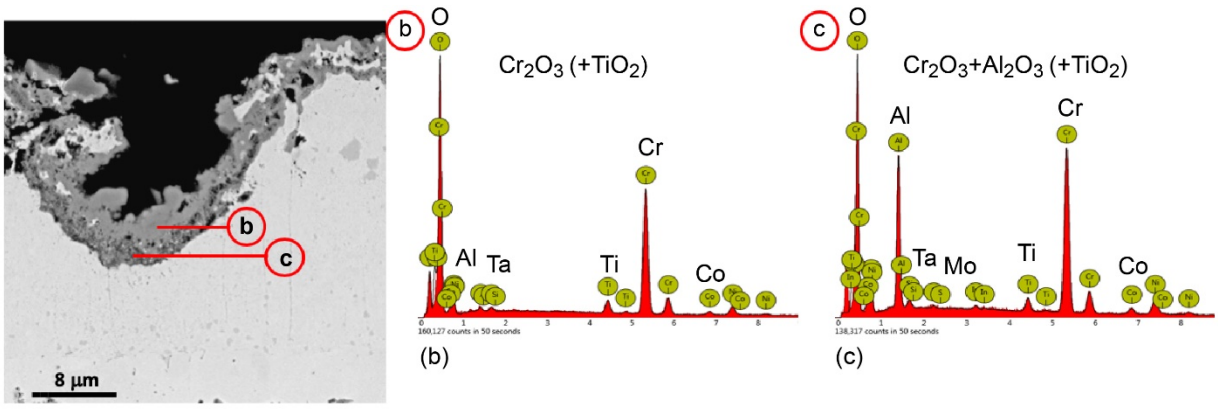

(a)

Figure 29.—(a) BSE image of the ***High Cr, Thin*** coating after LCF testing following oxidation and hot corrosion exposures showing the corrosion product in a cavity from a lost spit. (b,c) EDS spectra showing primarily Cr_2O_3 in the outer region and a mix of Cr_2O_3 and Al_2O_3 in the inner region.

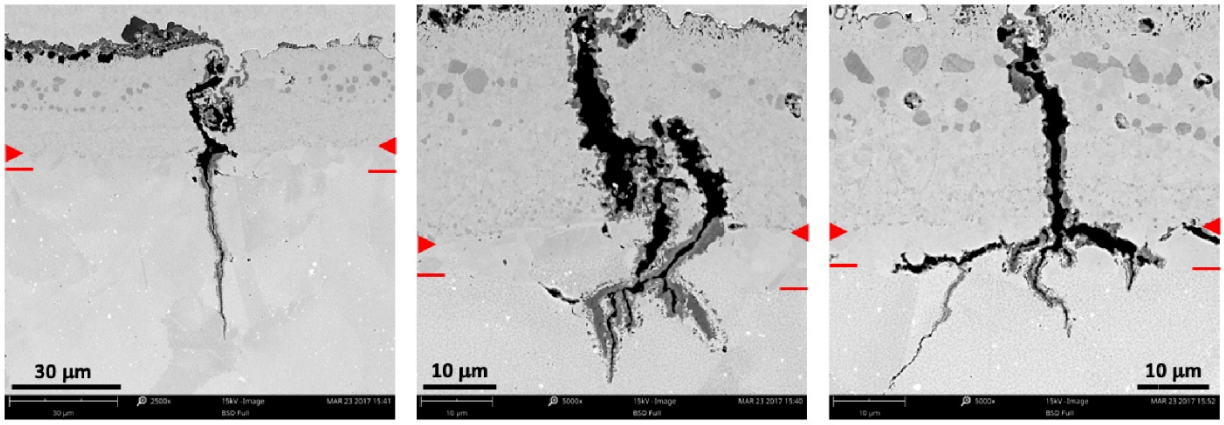

(a) (b) (c)

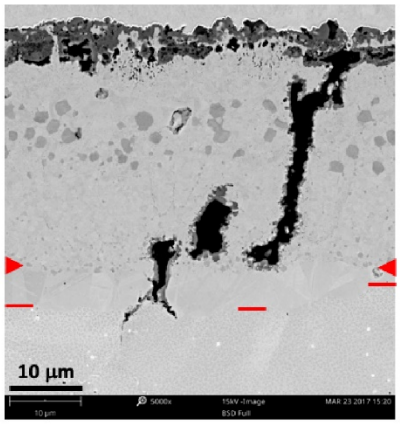

(d)

Figure 30.—(a-d) BSE images of the ***High Cr, Thin*** coating after LCF testing following oxidation and hot corrosion exposures showing fatigue cracks penetrating the coating and the disk alloy. Red arrowheads indicate the original C/S interface. Mounts were polished in the direction parallel to the specimen load axis (horizontal in the figure) to reveal fatigue cracks.

Microstructures of the ***Low Cr***, ***Thick*** coating are shown in Figure 31(a) and (b). The cracks show some tendency to follow the C/S interface or to branch, which again is likely the result of some compressive residual stress in the disk alloy. Earlier studies showed that residual stresses remained compressive after 35,000 cycles at 760 °C, however, this equates to only 37.2 h exposure at 760 °C (including an 8 h low PO_2 anneal) (Ref. 13) whereas this ***Low Cr***, ***Thick*** specimen has been exposed to more than 550 h at 760 °C. The weak bond between the ***Med Cr***, ***Thick*** coating and substrate is evident in Figure 31(c). Crack blunting at the C/S interface for the ***Med Cr+ZrO₂*** coating is shown in Figure 32(a) and (b). Except for the fatigue cracks, the ZrO_2 outer layer (bright) appears intact on the surface with the primarily Cr_2O_3 layer immediately below the ZrO_2 (Figure 32(c)).

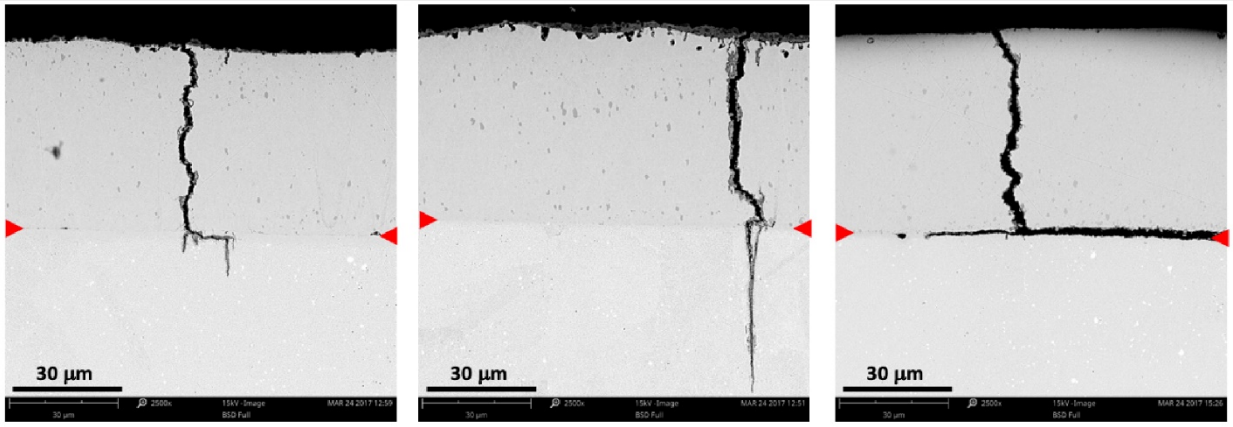

(a) (b) (c)

Figure 31.—BSE images of (a,b) the ***Low Cr, Thick*** coating, and (c) ***Med Cr, Thick*** coating after LCF testing following oxidation and hot corrosion exposures. Mounts were polished in the direction parallel to the specimen load axis (horizontal in the figure) to reveal fatigue cracks. Red arrowheads indicate the original C/S interface.

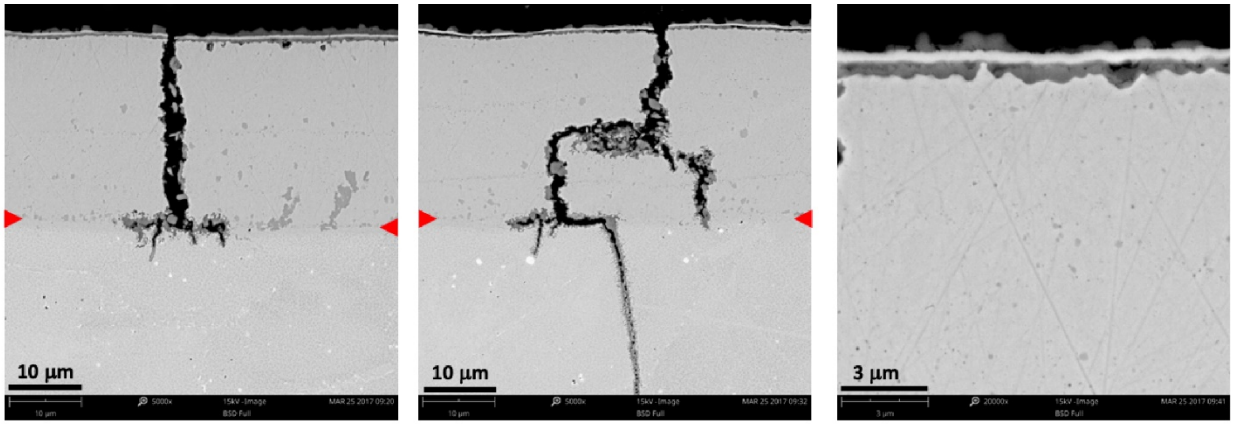

(a) (b) (c)

Figure 32.—(a-c) BSE images of the ***Med Cr+ZrO₂***, Thin coating after LCF testing following oxidation and hot corrosion exposures. Note the crack branching at the C/S interface. (c) indicates no corrosion penetration into the coating. Mounts were polished in the direction parallel to the specimen load axis (horizontal in the figure) to reveal fatigue cracks. Red arrowheads indicate the original C/S interface.

Discussion

The benefit of a coating for turbine disks can only be assessed by comparing the LCF lives of coated and uncoated specimens after an appropriate environmental exposure. The average life of the two uncoated specimens after oxidation and hot corrosion attack, shown by the dashed gray line and short black horizontal arrow in Figure 24, was 18,800 cycles. The average life with the two ***High Cr***, ***Thin*** coating was 36,501 cycles, almost double (1.94X) the average life of the uncoated specimens. Not surprisingly, the coating with the poor bond to the substrate (***Med Cr***, ***Thick***) performed worse after environmental exposures than the uncoated specimens. The other three coatings (***Med Cr***, ***Thin***; ***Low Cr***, ***Thick***; ***Med Cr+ZrO_2***, ***Thin***) all gave average lives better than the uncoated specimens (26,745, 25,423, and 24,714 cycles, respectively) but with only 32 to 42 percent improvement. It should also be noted that although the surface of the coating was sometimes exposed after the hot corrosion attack, no pits were observed in any coating. Hence, for the environmental and LCF conditions used in this study, all of the coatings, with the exception of the poorly bonded ***Med Cr***, ***Thick*** coating, were able to provide some protection with average lives between 1.3X to nearly 2X that of the uncoated specimens.

However, as in Reference 1, the reason for the consistently high LCF life with the ***High Cr***, ***Thin*** coating is unclear. There were no obvious corrosion pits in any of the coatings, and the polished microstructures shown in Figure 27 and Figure 31 do not show any noteworthy signs of corrosive attack in either the ***Low Cr*** or ***Med Cr*** coatings. Furthermore, the ***High Cr*** coating showed the highest lifetimes without environmental exposures in both the as-coated and annealed condition (Ref. 1), and after shot peening (above) while consistently exhibiting the largest amount of fatigue cracks in the coating (Figure 8 and Figure 25). Therefore, these observations would suggest that the superior LCF behavior of the ***High Cr*** coating may not be due solely to the better environmental protection afforded by the higher Cr level. It was suggested in Reference 1 that this coating has the highest strength due to the higher Cr concentration. However, since the coating appears to crack more readily during LCF testing, it is not clear how this higher strength benefits the LCF life. It can be hypothesized that the higher strength coating could "transmit" more of the shot peening energy to the substrate, where it can produce compressive residual stresses that are greater in magnitude and longevity.

It is apparent that the different coatings showed different levels of improvement with shot peening. For the thin coatings (***Low Cr***, ***Med Cr***, ***High Cr***), improvement in life scaled indirectly with the Cr content such that the ***Low Cr*** coating improved the most and the ***High Cr*** coating improved the least , as indicated by the blue arrows in Figure 6. The ***Med Cr+ZrO_2***, ***Thin*** coating improved similarly to the ***Med Cr***, ***Thin*** coating. The thicker coatings did not fit this pattern since the ***Low Cr***, ***Thick*** coating improved only a moderate amount, whereas the ***Med Cr***, ***Thick*** coating improved more than any other coating. This latter observation was the most surprising since the ***Med Cr***, ***Thick*** coating was shown both above and in Reference 1 to have a poor bond with the substrate becoming largely unattached during testing. It is suggested that the poor bond caused these specimens to behave largely as uncoated specimens without the detrimental defects of the coating. Cracks in the coating were simply arrested by delamination of the coating, as shown in Figure 31(c). However, with the extended oxidation and hot corrosion exposures, the coating provided no protection and the specimens exhibited lives as poor as or worse than the uncoated specimens.

It is interesting that shot peening showed no effect on the uncoated specimens (Figure 6, circle symbols). Recent work has shown that as-machined specimens possess a small compressive residual stress at the surface which becomes much more compressive after shot peening (Ref. 13). However, Gibson et al. (Ref. 22), discussed the tradeoffs with shot peening stating that the benefits of the near-surface strain hardening need to be weighed against the increased surface roughness which can result in an LCF life debit. The increase in roughness due to shot peening of the compositionally-similar disk

alloys ME3 and LSHR has also been reported previously (Refs. 9 and 13). In addition, peening introduces cold work in the peened specimen which, if excessive, can also degrade the fatigue life (Ref. 4). Hence, the lack of an increase in the LCF life after shot peening of the uncoated specimens might be due, in part, to an increase in surface roughness, or a detrimental amount of cold work in the specimen. The present fatigue test conditions had been chosen where prior data for uncoated specimens indicated a preference for fatigue failures to initiate at the surface. The failures of the two uncoated specimens that had been shot peened were at the surface, as for coated and shot peened specimens.

In Reference 1, without any shot peening, it was seen that the LCF life increased with the Cr concentration of the coating, as shown for the ***Low***, ***Med*** and ***High Cr***, ***Thin*** coatings in Figure 6 (open symbols). It was suggested that this increase in LCF life of these thin coatings might be due to the strength of the coating since the strength is expected to increase with Cr content. If the "coating" can be considered the outer 15 to 20 μm layer of a specimen, then the strongest "coating" would be for the case of the uncoated superalloy. As the strength of the coating (e.g., the near surface layer) increased, the LCF life also increased. After shot peening, the benefit of the shot peening decreased with increasing strength. In this scenario, the uncoated specimens fit this pattern with the thin coatings by having the highest LCF lives but experiencing the least benefit from shot peening. Although there is a clear pattern of a decreasing benefit due to shot peening with increasing coating strength, the cause for this pattern is unclear. Nevertheless, it is apparent that the shot peening had a beneficial effect on all of the coated specimens.

Although it is well known that the residual compressive stress imparted by shot peening can be greatly diminished by thermal excursions (Refs. 4, 9, 12, 13, and 23), it appears that some of the benefit remains in the substrate below the coating in the present study. Even though it was apparent that more fatigue cracks form in the coating than on the surface of uncoated specimens, most of the cracks continue to be arrested at the C/S interface in the coated specimens (Figure 27(b)). Some of the cracks showed branching at this interface which likely dissipated some of the energy and reduced the crack growth rate. Furthermore, some of the branched cracks were heavily oxidized which others have argued also dissipates energy associated with the crack (Ref. 24). Hence, although the LCF lives decreased due to either/both the long thermal exposures (550 h at 760 °C) and/or the oxidation and hot corrosion attack, the shot peening and residual compressive stress appears to have some beneficial impact on the crack propagation.

Although shot peening improved the LCF life of all coated specimens, fatigue cracks continued to initiate at spits or holes, identical to the behavior observed in Part I. As such, the spits behave similarly to large inclusions at the surface with a very detrimental impact on the LCF life (Refs. 4, 5, and 7). Obviously the plastic deformation of the spits did not bond or weld the spits to the surrounding coating. Oxidation along the bond line of spits indicated the poor bond remained after shot peening. Consequently, eliminating the spits (and thereby the holes) during coating fabrication should be a priority.

It is obvious that diffusional transport, even for relatively short times (30 to 50 h) at 760 °C, leads to significant transport of Al and Ti from the substrate to the coating surface. The selective oxidation of these elements is expected based on Gibbs free energy arguments (Ref. 25). Diffusion rates in the coating may be enhanced due to the significant strain energy stored in the coating after shot peening. Al diffusion leading to Al_2O_3 formation as "fingers" growing into the coating has previously been reported for a slightly thinner (12 to 14 μm) ***Med Cr*** coating after 500 and 1020 h at 760 °C (Ref. 20). In the present study, although Al is primarily detected at shorter times (30 to 50 h), Ti is obviously present in the oxide scale after 550 h of oxidation and hot corrosion exposure, especially in the ***High Cr*** coating (Figure 13). However, the significant presence of the Ti in the ***High Cr*** coating after 500 h of oxidation, for which the only source is the substrate, but not in the ***Low*** or ***Med Cr*** coatings (Figure 12), is puzzling. However, the detection of Ti on the surface but not Al is not surprising. Aluminum, being more oxygen active than Cr or Ti, would be expected to form Al_2O_3 at lower oxygen pressures below the external oxide

scale. The porous subscale region, below the outer Cr_2O_3 (TiO_2) scale, could also contain some Al_2O_3. Hence, it is not unexpected that Cr_2O_3 and TiO_2 were detected by EDS on the surface of the outer scale, with Al_2O_3 only detected on polished cross sections below the external scale, or in the subscale.

Although Al and Ti appear to readily diffuse from the substrate to the coating, there appears to be limited Cr transport from the coating to the surface. Chromium in the coating is obviously being selectively oxidized to form a nearly continuous protective scale of Cr_2O_3 on the surface. This is consistent with the observation of primarily Cr_2O_3 formation after extended cyclic oxidation (1,020 of 1-h cycles) of a ***Med Cr*** Ni-35Cr-0.15Y coating at 760 °C (Ref. 20). The Cr_2O_3 scale appears only disrupted by pores, cracks and defects (e.g., spits). However, there is no significant recession of the α-Cr phase near the surface, even after 500 h of oxidation (Figure 16(b) and Figure 18(a)) for all three coating compositions. This lack of recession indicates a low rate of Cr consumption and low growth rate of Cr_2O_3 during oxidation. During hot corrosion of the ***Med Cr*** coating, the Cr consumption rate again appears low since there are α-Cr particles near the external Cr_2O_3-MgO external scale (Figure 27(a) and (c). However, there appears to be a layer depleted of the α-Cr phase in the ***High Cr***, ***Thin*** coating after hot corrosion (Figure 28(a) to (c)). This would suggest a higher rate of Cr consumption leading to the recession of this high-Cr phase. In contrast, a high rate of Cr diffusion in the lower Cr disk substrate results in the large α-Cr recession from the C/S interface to nearly the center of the coating, as shown in Figure 17, Figure 28(a), Figure 30(a) and (d) and as observed previously (Ref. 20).

A higher rate of Cr consumption in the ***High Cr***, ***Thin*** coating than that in the ***Med Cr***, ***Thin*** coating could help explain the multi-layered oxide scale observed in the ***High Cr*** coating (Figure 28). In the ***Med Cr***, ***Thin*** coating, it appears that Cr diffusion to the oxide scale has resulted in a near continuous layer of porosity in the near-surface region of the coating (Figure 27(a)). This layer clearly shows oxide within this porosity suggesting that oxygen has accessed the porosity, and that large sections of the porosity have linked. Oxygen access to the porosity could be the result of fatigue cracks, or simply cracking of the scale. This oxidation of the pores has trapped a thin layer of metal between the external scale and the oxidized porosity (Figure 27(a)). The layer of oxidized porosity would function as the external scale with growth of Cr_2O_3 in the pores. If this same process occurs at a higher rate of Cr with the ***High Cr***, ***Thin*** coating, a new layer of connected porosity could form below the first layer of oxidized porosity and eventually develop the multilayered scale shown in Figure 28(a) to (c) where there are three distinct layer of oxide containing pores Figure 28(c). Although this discussion above could help explain the morphology of the multilayered scale in the ***High Cr***, ***Thin*** coating, it does not explain why the ***High Cr***, ***Thin*** coating shows the highest LCF life.

In both Reference 1 and the present study, the ***High Cr***, ***Thin*** coating consistently yielded the highest LCF lives of all the examined coatings. However, because of the high amount of cracking in this coating, these results could be misleading if hot corrosion attack were allowed to occur during the LCF testing. Since cracking only occurs during LCF tests, performing hot corrosion testing simultaneously with the LCF testing would allow molten salt attack into the numerous cracks in the coating with the potential of attack into the substrate. As stated above, the sequential nature of the testing in this study allowed only oxidation attack during the LCF testing due to removal of all salts and corrosion product prior to LCF testing. Work elsewhere has shown that leaving the corrosion product on the surface during LCF testing resulted in corrosive attack in the cracks and into the substrate when the LCF testing followed corrosion exposure (Refs. 26 and 27). Hence, allowing the salt and corrosion products to remain on the surface during the LCF testing could increase the severity of the test and might affect the findings in this study. Limited corrosion tests of specimens coated with one of the present coatings using the PEMS process, possessing coating cracks produced by unloaded thermal cycling, did not subsequently display increased corrosion rates or pitting at the cracks when corrosion tested (Ref. 20).

There are obvious shortcomings in the current test procedures where the extended oxidation exposure, hot corrosion, and LCF testing is performed in a sequential manner. First, the hot corrosion attack might not be as severe because a protective oxide scale had been allowed to form and grow during the 500 h oxidation exposure. However, most aircraft engines, if experiencing any hot corrosion attack during takeoff and landings in certain airports, would likely also be experiencing periods consisting only of oxidation. In addition, other studies have found that cracking in thick, brittle oxide scales initiates fatigue cracks which is why environmental attack often leads to surface initiated cracking (Refs. 24, 26 to 28). Removing the water soluble salts and corrosion products prior to LCF testing likely also makes a significant impact on the test results. Sonic washing of the surface after hot corrosion results in eliminating corrosive attack from occurring during the fatigue testing which, as stated above, removes any possibility of corrosive attack in the cracks and into the more susceptible substrate. Fatigue studies have been carried out by other groups in a closed chamber in the presence of SO_2 gas and with various salts on the specimen surface (Refs. 29 to 31). In some of these tests which were conducted on Ni-base alloys without coatings, corrosion attack under the right stress and salt loading conditions resulted in more detrimental V-shaped pits which decreased the LCF life (Refs. 29 and 30). The test procedure in the current study requiring a water wash prior to LCF testing was selected early in the program as a way to identify any pit formation following hot corrosion since pits had been identified as crack initiation sites. It was also known that the Na-Mg sulfate salt being used was molten at the test temperature of 760 °C. Performing hot corrosion in a horizontal furnace prior to LCF testing with the specimens held in a horizontal position limited the flow of the salt to the test section of the LCF specimens and eliminated the possibility of molten salt flowing into and causing damage in the specimen grips of the LCF test frame. Although no pits have been observed in any NiCr-Y-coated test specimens, the test protocol remained fixed to allow comparisons between current and previous testing. Although an environmental chamber is required to allow hot corrosion attack with a known SO_2-containing gas during the LCF testing, simply allowing the corrosion product to remain on the surface during LCF testing would be a more realistic and harsh environment. If the corrosion product were to be left on the surface, sufficient salt should be applied, or resupplied during the test, to provide an adequate supply of reactants during the LCF test.

Conclusions

1. All of these coatings (with the exception of the poorly bonded ***Med Cr***, ***Thick*** coating), can provide protection from oxidation and hot corrosion, with average LCF lives spanning 1.3X to nearly 2X that of uncoated specimens.
2. The coating with the highest Cr content can exhibit the highest LCF life after shot peening, and after environmental exposures.
3. Corrosion pits can be avoided on the surface of these coatings for the present test conditions, after suitable processing.
4. Shot peening can be used to increase the LCF life of specimens with these coatings.
5. Spits and holes in the coating can remain after shot peening, and can act as crack initiation sites.
6. After shot peening, anneal, and optional oxidation and hot corrosion the present test conditions can encourage most primary cracks to eventually initiate at the surface, allowing consistent comparisons for the effects of surface integrity on fatigue life.
7. Al and Ti can rapidly diffuse from the substrate through these coatings and participate in oxidation on the coating surface (Ti) or in the near-surface subscale region (Al) for these test conditions. As expected, Cr consumption can be higher during hot corrosion than oxidation.

References

1. J.A. Nesbitt, T.P. Gabb, S.L. Draper, R.A. Miller, I.E. Locci, and C.K. Sudbrack, "LCF Life of As-Deposited and Annealed NiCr-Y Coatings for Oxidation and Hot Corrosion Protection of Disk Alloys," NASA/TM—2019-220340, Washington, D.C., November 2019.
2. S. Bashir, P. Taupin, and S.D. Antolovich, "Low cycle fatigue of as-HIP and HIP+ forged René 95," Metallurgical Transactions A 10 (10), 1481–1490 (1979).
3. D.R. Chang, D.D. Krueger, and R.A. Sprague, "Superalloy Powdier Processing, Properties and Turbine Disk Applications," Superalloys 1984, ed. M. Gell, The Minerals, Metals & Materials Society, Warrendale, PA, pp. 245–273 (1984).
4. R.L. Barrie, T.P. Gabb, J. Telesman, P.T. Kantzos, A. Prescenzi, T. Biles, and P.J. Bonacuse, "Effectiveness of shot peening in suppressing fatigue cracking at non-metallic inclusions in Udimet® 720," Materials Science and Engineering: A 474 (1–2), 71–81 (2008).
5. P. Kantzos, P. Bonacuse, J. Telesman, T.P. Gabb, R. Barrie, and A. Banik, "Effect of Powder Cleanliness on The Fatigue Behavior of Powder Metallurgy Ni-Disk Alloy Udimet 720," Superalloys 2004, The Minerals, Metals & Materials Society, Warrendale, PA, pp. 409–417 (2004).
6. D.M. Mattox, "Handbook of physical vapor deposition (PVD) processing: film formation, adhesion, surface preparation and contamination control," Noyes Publications; ISBN: 0-8155-1422-0, pp. 471–474 (1998).
7. T.P. Gabb, J. Telesman, P.T. Kantzos, P.J. Bonacuse, and R.L. Barrie, "Initial Assessment of the Effects of Nonmetallic Inclusions on Fatigue Life of Powder-Metallurgy-Processed Udimet (R) 720," NASA/TM-2002-211796, Washington, D.C., August, 2002.
8. T.P. Gabb, J. Telesman, B. Hazel, and D.P. Mourer, "The Effects of Hot Corrosion Pits on the Fatigue Resistance of a Disk Superalloy," Journal of Materials Engineering and Performance 19 (1), 77–89 (2009).
9. T.P. Gabb, A. Dianetti, S.L. Draper, I.E. Locci, and J. Telesman, "Retention of Compressive Residual Stresses Introduced by Shot Peening in a Powder Metal Disk Superalloy," NASA TM—2016-219414, Washington, D.C., December, 2016.
10. B.J. Foss, S. Gray, M.C. Hardy, S. Stekovic, D.S. McPhail, and B.A. Shollock, "Analysis of Shot-Peening and Residual Stress Relaxation in the Nickel-based Superalloy RR1000," Acta Materialia 61 (7), 2548–2559 (2013).
11. A. Evans, S. Kim, J. Shackleton, G. Bruno, M. Preuss, and P. Withers, "Relaxation of Residual Stress in Shot Peened Udimet 720Li under High Temperature Isothermal Fatigue," International Journal of Fatigue 27 (10–12), 1530–1534 (2005).
12. T.P. Gabb, J. Telesman, P.T. Kantzos, P.J. Bonacuse, R.L. Barrie, and D.J. Hornbach, "Stress Relaxation in Powder Metallurgy Superalloy Disks," TMS Letters 5, 115–116 (2004).
13. T.P. Gabb, R.B. Rogers, J.A. Nesbitt, R.A. Miller, B.J. Puleo, D. Johnson, J. Telesman, S.L. Draper, and I.E. Locci, "Influences of Processing and Fatigue Cycling on Residual Stresses in a NiCrY-Coated Powder Metallurgy Disk Superalloy," Journal of Materials Engineering and Performance 26 (11), 5237–5250 (2017).
14. J. Neumann, "Development of Ductile Coatings to Protect Advanced Powder Metallurgy (PM) Alloy Turbine Disks From Hot Corrosive Attack," Honeywell Aerospace Contract NNC08CA62C, Phoenix, AZ, 2010.
15. J.A. Nesbitt and S.L. Draper, "Pit Morphology and Depth after Low-Temperature Hot Corrosion of a Disc Alloy," Materials at High Temperatures 33 (4–5), 501–516 (2016).

16. Phase Equilibria Diagrams, in CD-ROM Database, Version 3.3.0, T.A.C.S. (ACerS), Editor. 2010, The American Ceramic Society (ACerS), 600 N. Cleveland Ave., Suite 210, Westerville, Ohio 43082.
17. T.P. Gabb, J. Telesman, P.T. Kantzos, and A. Garg, "Effects of Temperature on Failure Modes for a Nickel-Base Disk Superalloy," Journal of Failure Analysis and Prevention **7** (1), 56–65 (2007).
18. C.K. Sudbrack, S.L. Draper, T.T. Gorman, J. Telesman, T.P. Gabb, and D.R. Hull, "Oxidation and the Effects of High Temperature Exposures on Notched Fatigue Life of an Advanced Powder Metallurgy Disk Superalloy," Superalloys 2012, ed. E.S. Huron, R.C. Reed, M.C. Hardy, M.J. Mills, R.E. Montero, P.D. Portella, J. Telesman, The Minerals, Metals & Materials Society, Warrendale, PA, 2012, pp. 863–872.
19. T.P. Gabb, C.K. Sudbrack, S.L. Draper, R.A. MacKay, and J. Telesman, "Effects of Long Term Exposures on PM Disk Superalloys," NASA/TM—2013-216614, Washington, D.C., December 2013.
20. T.P. Gabb, R.A. Miller, C.K. Sudbrack, S.L. Draper, J.A. Nesbitt, R.B. Rogers, J. Telesman, V. Ngo, and J. Healy, "Cyclic Oxidation and Hot Corrosion of NiCrY-Coated Disk Superalloys," NASA/TM—2016-219105, Washington, D.C., June 2016.
21. A. Encinas-Oropesa, G.L. Drew, M.C. Hardy, A.J. Leggett, J.R. Nicholls, and N.J. Simms, "Effects of oxidation and hot corrosion in a nickel disc alloy," Superalloys 2008, ed. R.C. Reed, K.A. Green, P. Caron, T.P. Gabb, M.G. Fahrmann, E.S. Huron, S.A. Woodard, The Mining, Metallurgy, and Materials Society, Warrendale, PA, pp. 609–618 (2008).
22. G.J. Gibson, K.M. Perkins, S. Gray, and A.J. Leggett, "Influence of Shot Peening on High-Temperature Corrosion and Corrosion-Fatigue of Nickel Based Superalloy 720Li," Materials at High Temperatures 33 (3), 225–233 (2016).
23. M.R. Bache, J.P. Jones, G.L. Drew, M.C. Hardy, and N. Fox, "Environment and Time Dependent Effects on the Fatigue Response of an Advanced Nickel Based Superalloy," International Journal of Fatigue 31 (11–12), 1719–1723 (2009).
24. X. Yang, S. Li, and H. Qi, "Effect of MCrAlY Coating on the Low-Cycle Fatigue Behavior of a Directionally Solidified Nickel-Base Superalloy at Different Temperatures," International Journal of Fatigue 75, 126–134 (2015).
25. H.S. Kitaguchi, H.Y. Li, H.E. Evans, R.G. Ding, I.P. Jones, G. Baxter, and P. Bowen, "Oxidation Ahead of a Crack Tip in an Advanced Ni-Based Superalloy," Acta Materialia 61 (6), 1968–1981 (2013).
26. S. Li, X. Yang, H. Qi, G. Xu, and D. Shi, "Influence of MCrAlY Coating on Low-Cycle Fatigue Behavior of a Directionally Solidified Nickel-Based Superalloy in Hot Corrosive Environment," Materials Science and Engineering: A 678, 57–64 (2016).
27. H. Qi, J. Yang, X. Yang, S. Li, and L. Ma, "Fatigue Behavior of Uncoated and MCrAlY-Coated DS Nickel-Based Superalloys Pre-Exposed in Hot Corrosion Condition," Rare Metals 37 (11), 936–941 (2017).
28. S. Li, H. Qi, and X. Yang, "Oxidation-Induced Damage of an Uncoated and Coated Nickel-Based Superalloy under Simulated Gas Environment," Rare Metals 37 (3), 204–209 (2018).
29. H.L. Cockings, K.M. Perkins, and M. Dowd, "Influence of Environmental Factors on the Corrosion-Fatigue Response of a Nickel-Based Superalloy," Materials Science and Technology 33 (9), 1048–1055 (2017).
30. D.J. Child, J. Meldrum, and P. Onwuarolu, "Corrosion-Fatigue Testing of Ni-Based Superalloy RR1000," Materials Science and Technology 33 (9), 1040–1047 (2017).
31. H. Rosier, K. Perkins, A. Girling, J. Leggett, and G. Gibson, "Factors Affecting the Corrosion Fatigue Life in Nickel based Superalloys for Disc Applications," MATEC Web of Conferences, 14, p. 03001. EDP Sciences, 2014.

Appendix—Alloy, Coating Designation, Cr Content in weight percent (wt%), Thickness and LCF Life, Total Time at 760 °C

Alloy	Coating designation	Cr, wt%	ΔX, μm	Low PO_2	SP	OX	HC	LCF life, cycles	LCF test time, h	Total time at 760 °C, h	Specimen ID
LSHR	Uncoated	-	-	N	N	N	N	55,123	45.9	45.9	T3-L17
LSHR	Uncoated	-	-	N	N	N	N	46,025	38.4	38.4	U3-L1
LSHR	Uncoated	-	-	N	N	N	N	49,879	41.6	41.6	Z6-L14
ME3	Uncoated	-	-	Y	Y	N	N	51,844	43.2	51.2	M3-101
ME3	Uncoated	-	-	Y	Y	N	N	52,183	43.5	51.5	M3-160
LSHR	Low Cr, Thin	29	20	Y	N	N	N	11,833	9.9	17.9	NM1, U3-L3
LSHR	Low Cr, Thin	"	"	Y	N	N	N	13,201	11.0	19.0	NM1, U3-L4
ME3	Low Cr, Thin	"	"	Y	N	N	N	11,362	9.5	17.5	NM1, M3-2
ME3	Low Cr, Thin	"	"	Y	N	N	N	15,371	12.8	20.8	NM1, M3-4
LSHR	Med Cr, Thin	37.0	21	Y	N	N	N	17,648	14.7	22.7	NM2, U3-L9
LSHR	Med Cr, Thin	"	"	Y	N	N	N	16,039	13.4	21.4	NM2, U3-L10
LSHR	High Cr, Thin	44	20	Y	N	N	N	32,161	26.8	34.8	NM4, U3-L17
LSHR	High Cr, Thin	"	"	Y	N	N	N	33,979	28.3	36.3	NM4, U3-L18
LSHR	Low Cr, Thick	29	38	Y	N	N	N	9,878	8.2	16.2	NM3, U3-L11
LSHR	Low Cr, Thick	"	"	Y	N	N	N	10,090	8.4	16.4	NM3, U3-L12
LSHR	Med Cr, Thick	35	41	Y	N	N	N	11,000	9.2	17.2	NM6, U3-L21
LSHR	Med Cr, Thick	"	"	Y	N	N	N	11,755	9.8	17.8	NM6, U3-L22
LSHR	Med Cr+ZrO_2, Thin	35	19	Y	N	N	N	15,452	12.9	20.9	NM7, U3-L25
LSHR	Med Cr+ZrO_2, Thin	"	"	Y	N	N	N	18,600	15.5	23.5	NM7, U3-L26
ME3	Low Cr, Thin	29	20	Y	Y	N	N	32,650	27.2	35.2	NM1, M3-5
ME3	Low Cr, Thin	"	"	Y	Y	N	N	33,311	27.8	35.8	NM1, M3-31
ME3	Med Cr, Thin	37.0	21	Y	Y	N	N	32,311	26.9	34.9	NM2, M3-34
ME3	Med Cr, Thin	"	"	Y	Y	N	N	31,237	26.0	34.0	NM2, M3-37
ME3	High Cr, Thin	44	20	Y	Y	N	N	48,732	40.6	48.6	NM4, M3-55
ME3	High Cr, Thin	"	"	Y	Y	N	N	41,560	34.6	42.6	NM4, M3-59
ME3	Low Cr, Thick	29	38	Y	Y	N	N	17,505	14.6	22.6	NM3, M3-50
ME3	Low Cr, Thick	"	"	Y	Y	N	N	14,918	12.4	20.4	MN3, M3-54
ME3	Med Cr, Thick	35	41	Y	Y	N	N	35,826	29.9	37.9	NM6, M3-61
ME3	Med Cr, Thick	"	"	Y	Y	N	N	50,681	42.2	50.2	NM6, M3-64
ME3	Med Cr+ZrO_2, Thin	35	19	Y	Y	N	N	31,391	26.2	34.2	NM7, M3-139
ME3	Med Cr+ZrO_2, Thin	"	"	Y	Y	N	N	30,108	25.1	33.1	NM7, M3-162
ME3	Med Cr, Thin	37.0	21	Y	Y	Y	Y	27,640	23.0	31.0	NM2, M3-36
ME3	Med Cr, Thin	"	"	Y	Y	Y	Y	25,850	21.5	29.5	NM2, M3-46
ME3	High Cr, Thin	44	20	Y	Y	Y	Y	35,736	29.8	37.8	NM4, M3-56
ME3	High Cr, Thin	"	"	Y	Y	Y	Y	37,265	31.1	39.1	NM4, M3-58
ME3	Low Cr, Thick	29	38	Y	Y	Y	Y	22,313	18.6	26.6	NM3, M3- 51
ME3	Low Cr, Thick	"	"	Y	Y	Y	Y	28,532	23.8	31.8	MN3, M3-52
ME3	Med Cr, Thick	35	41	Y	Y	Y	Y	17,486	14.6	22.6	NM6, M3-63
ME3	Med Cr, Thick	"	"	Y	Y	Y	Y	5,807	4.8	12.8	NM6, M3-65
ME3	Med Cr+ZrO_2, Thin	35	19	Y	Y	Y	Y	29,932	24.9	32.9	NM7, M3-66
ME3	Med Cr+ZrO_2, Thin	"	"	Y	Y	Y	Y	19,496	16.2	24.2	NM7, M3- 195

Cr refers to the Cr content in wt% measured by EDS
ΔX refers to the thickness measured on pins after 16N-200 percent shot peen and 8 h low PO_2 diffusion anneal
Low PO_2 refers to the 8 h Low PO_2 diffusion anneal
SP refers to the 16N-200 percent shot peen treatment
OX refers to the 500 h oxidation exposure at 760 °C in air
HC refers to the 50 h hot corrosion exposure at 760 °C with salted surface, in air
LCF Life is the number of LCF cycles before failure
LCF Test Time is the time at 760 °C during LCF testing
Total time refers to the total time at 760 °C for that specimen